Citation for final published version:

Figure 1.

a. Mean annual dust deposition (kg/m²s)
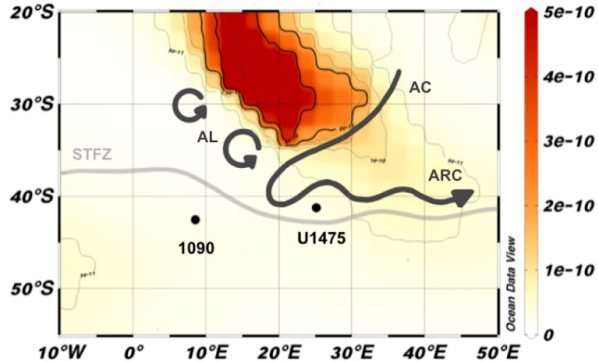
b. Mean annual surface nitrate (µmol/l)

Figure 2.

a. Modern/Interglacial   b. Fronts move north/Glacial   c. Frontal migration and Iron fertilization/Glacial

Figure 3.

N. pachyderma   *G. bulloides*   *G. inflata*

Figure 4.

Figure 5.

a.

b.

c.

Age (ka)

Figure 6.

1 **Glacial Southern Ocean expansion recorded in foraminifera-bound nitrogen**
2 **isotopes from the Agulhas Plateau during the Mid-Pleistocene Transition**

3 **B. A. Marcks[1]*, T. P. Dos Santos[2], D. V. O. Lessa[2], A. Cartagena-Sierra[3], M. A. Berke[3], A.**
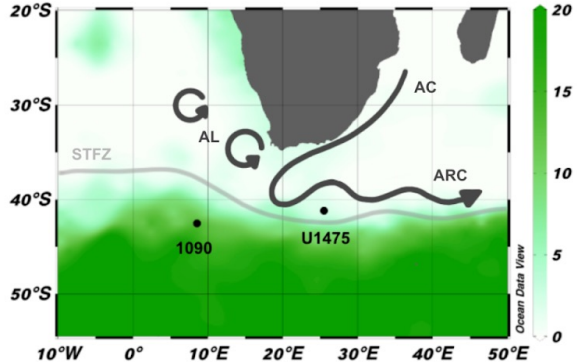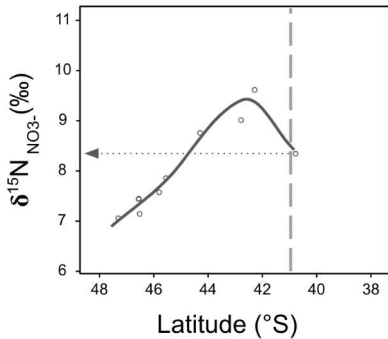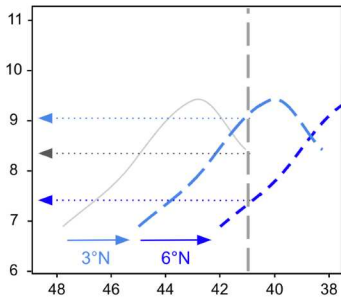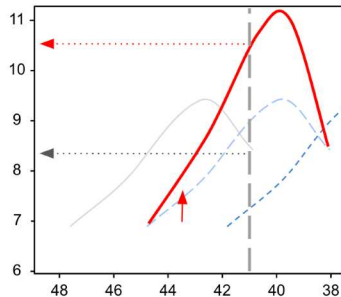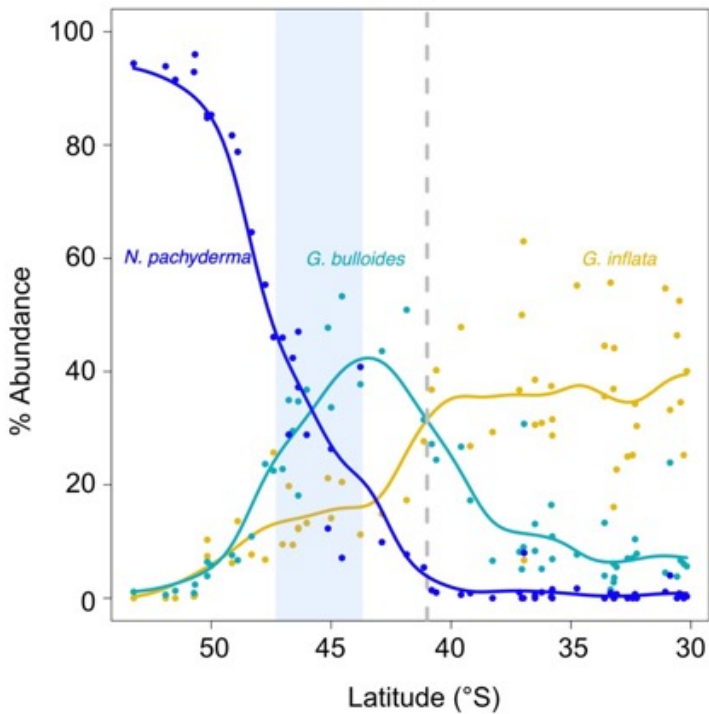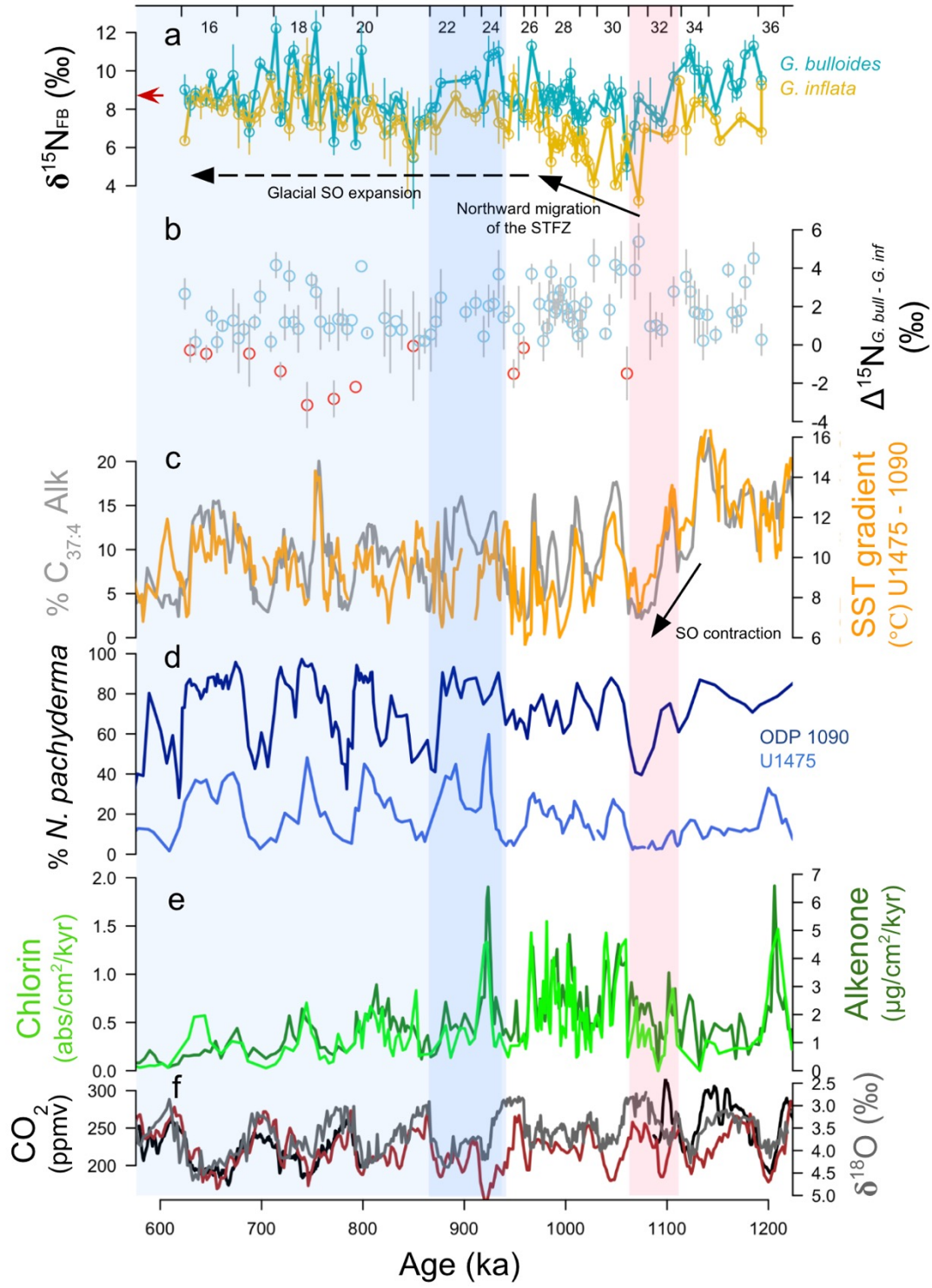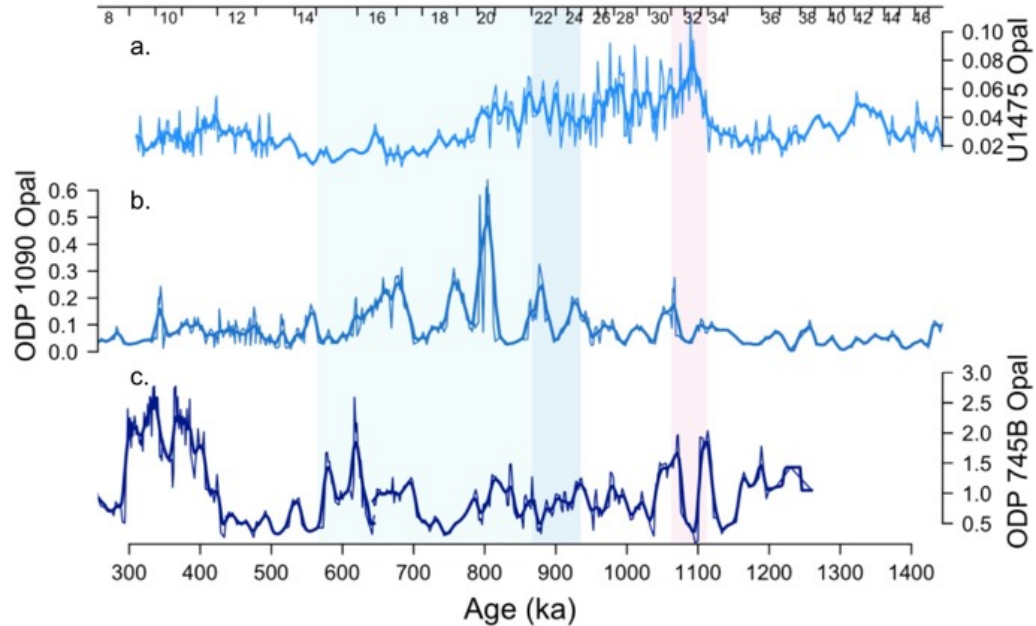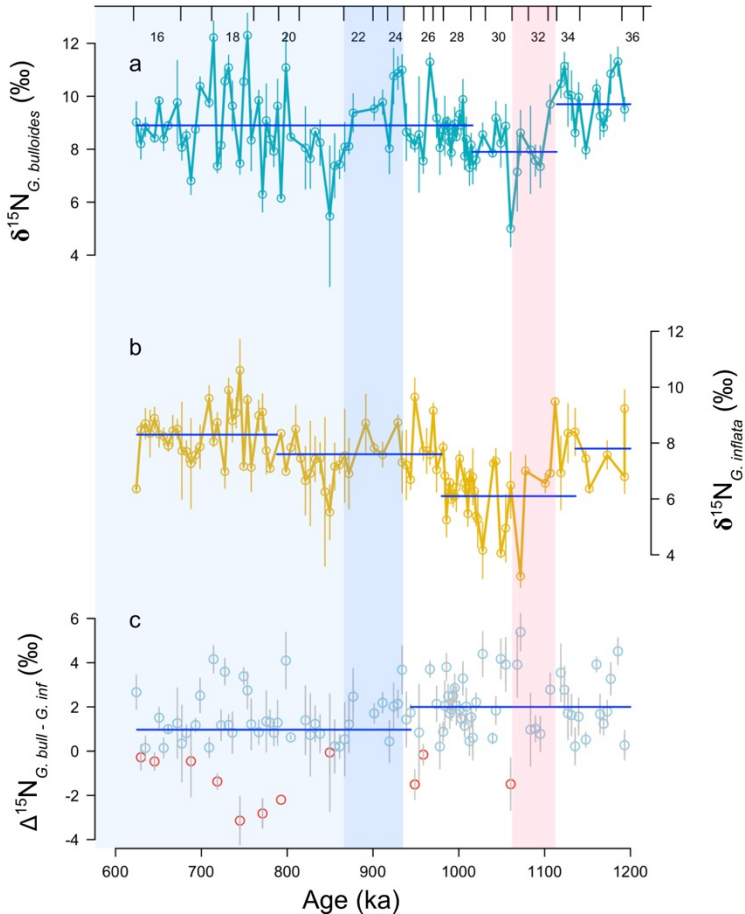4 **Starr[4], I. R. Hall[4], R. P. Kelly[1], R. S. Robinson[1]**

5 [1]Graduate School of Oceanography, University of Rhode Island, Narragansett, RI, USA.
6 [2]Programa de Pós-Graduação em Geoquímica Ambiental, Universidade Federal Fluminense,
7 Brazil.
8 [3]Department of Civil and Environmental Engineering and Earth Sciences, University of Notre
9 Dame, Notre Dame, IN, USA.
10 [4]School of Earth and Environmental Sciences, Cardiff University, Cardiff, UK.
11 *Corresponding author: Basia Marcks (bmarcks@uri.edu)

12 **Plain Language Summary:**

13 The Mid-Pleistocene Transition is a unique period of time, during which the natural rhythm of
14 Earth's climate shifted, the pace of glacial and interglacial cycles changed from 40,000 years to
15 100,000 years as ice sheets expanded, carbon accumulated in the deep ocean, and the planet
16 cooled. The exact cause of these changes is unclear, but internal system feedbacks were likely at
17 play. As climate changes today and the oceans increasingly take up carbon, the Mid-Pleistocene
18 Transition provides a unique case study to investigate Earth's natural climate system and
19 important carbon cycle feedbacks. In this paper we use the nitrogen isotopic composition of
20 plankton shells and other biogeochemical records to show that leading up to the Mid-Pleistocene
21 Transition the Southern Ocean underwent major physical changes and expanded as 100,000 year
22 glacial cycles emerged. Our data indicates that the expansion of the Southern Ocean delivered
23 cold, nutrient rich waters northward where they could mix with warm, salty Indian and Atlantic
24 Ocean waters as hypothesized by other studies.

25 **Key Points:**

26 • Foraminifera-bound nitrogen isotope values from the Agulhas Plateau record latitudinal
27 migrations of the Subtropical Front.

28 • Elevated foraminifera-bound nitrogen isotope values after 900 ka are consistent with Southern
29 sourced nitrate.

30 • Southern Ocean contraction during a "super interglacial" brings more subtropical nitrate to the
31 Agulhas Plateau.

32

33   **Abstract**

34   The emergence of 100-kyr glacial cycles (The Mid-Pleistocene Transition, MPT) is attributed in

35   part to slower global overturning circulation and iron stimulation of biological carbon drawdown

36   in the Southern Ocean. We present foraminifera-bound nitrogen isotope values and polar

37   planktic foraminifera abundances from the Agulhas Plateau that show that increases in biogenic

38   sediment accumulation coincide with northward migrations of the Subtropical Frontal Zone

39   (STFZ) and elevated foraminifera-bound nitrogen isotope values during MPT glacial episodes.

40   The nitrogen isotope values of two planktic foraminifera species, *Globigerina bulloides* and

41   *Globorotalia inflata* show remarkable coherence amongst the sea surface temperature gradient

42   between the STFZ and SAZ, and polar foraminifera abundances, indicating a strong relationship

43   between nitrogen isotope dynamics above the Agulhas Plateau and migrations of the STFZ.

44   Northward migration of the STFZ may have been essential to prolonging glacial intervals by

45   increasing deep ocean carbon storage via a northward shift of the South Westerly Winds (SWW)

46   and a reduction in upwelling, delivery of fresher surface waters into the upper limb of global

47   overturning circulation, or inhibiting heat and salt delivery to the Atlantic as Agulhas Leakage.

48   **1 Introduction**

49   Around 1 million years ago (Ma), Antarctica and the Southern Ocean witnessed expansion of

50   polar ice sheets and Southern Ocean sea ice (Starr et al., 2021) and increases in iron delivery and

51   biological productivity in the Subantarctic Zone (SAZ) (Martínez-García et al., 2009; Kemp et

52   al., 2010). Alongside evidence for increased deep ocean carbon storage (Farmer et al., 2019),

53   these surface changes implicate a Southern Ocean driver in the extension and amplification of

54   glacial-interglacial cycles from 40 kyr to ~100 kyr pacing during the MPT (1,200 - 600 ka)

55   (Chalk et al., 2017; Hönisch et al., 2009; Pena & Goldstein, 2014; Lear et al., 2016; Hoogakker

56   et al., 2006; Hasenfratz et al., 2019). Several hypotheses exist to explain the mechanisms

57   responsible for the MPT. Enhanced biological pump efficiency, increasing carbon export from

58   the surface (and atmosphere) to the deep ocean, as well as slower ocean circulation, reducing

59   CO_2 outgassing and extending the residence time of carbon in the deep ocean, have been

60   proposed. However, without evidence demonstrating an increase in Southern Ocean nutrient

61   consumption, the relative importance of each process in reducing glacial atmospheric CO_2 across

62   the MPT remains ambiguous (Martínez-García et al., 2009; Diekmann & Kuhn, 2002; Kemp et

63   al., 2010; Jaccard et al., 2013; Crundwell et al., 2008). Observed increases in biogenic sediment

64   accumulation in the glacial Southern Ocean SAZ across the MPT could result from iron

65   fertilization or Southern Ocean expansion in response to cooling and Antarctic ice sheet growth

66   (Martínez-García et al., 2009; Diekmann & Kuhn, 2002).

67   The evidence for the northward expansion of the Southern Ocean during the MPT comes from

68   the Atlantic Sector of the Southern Ocean (Kemp et al., 2010; Diekmann & Kuhn, 2002) and

69   more recently the Indian-Atlantic Ocean Gateway, south of Africa (Starr et al., 2021; Cartagena-

70   Sierra et al., 2021; Tangunan et al., 2021). Expansion of the Southern Ocean via northward

71   migrations of the STFZ and SWW slows global overturning circulation and increases deep ocean

72   carbon storage (Russell et al., 206; Toggweiler et al., 2006; Marshall & Speer, 2012; Ferrari et

73   al., 2014; Sigman et al., 2021). The Indian-Atlantic Ocean Gateway is globally significant due to

74   the eddies of salty Indian Ocean surface waters that are shed into the Atlantic Ocean as Agulhas

75   Leakage (AL). AL contributes excess salt to the surface return flow of the Atlantic Meridional
76   Overturning Circulation (AMOC) that is needed for deep convection and North Atlantic Deep
77   Water (NADW) formation (Pena & Goldstein, 2014; Caley et al., 2012; Beal et al., 2011).
78   Northward migrations of the STFZ have been proposed to cut off or limit AL on millennial and
79   glacial interglacial timescales as well as during the MPT. Evidence for significantly reduced AL
80   during intervals when the Antarctic Polar Front is thought to have moved at least 7 degrees
81   northward comes from the South Atlantic (Bard and Rickaby, 2009; Kemp et al., 2010; Caley et
82   al., 2012). Recent evidence for increased ice-rafted debris accumulation beneath the STFZ during
83   the early stages of glacial periods across the MPT suggests an expansion of cool, fresh SAZ
84   waters into the subtropics (Starr et al., 2021). This 'southern escape' of fresh water potentially
85   increased the buoyancy of the surface return flow of the AMOC, reducing NADW formation,
86   and slowing overturning (Starr et al., 2021; Pena & Goldstein, 2014). Whether by reducing salty
87   AL or adding fresh water via the southern escape, these changes provide a physical means of
88   carbon sequestration during the MPT (Starr et al., 2021; Simon et al., 2013). In this region, such
89   dramatic northward migrations of the Southern Ocean fronts would also deliver excess
90   macronutrients towards the subtropics, closer to South African and South American aeolian dust
91   sources (Martin, 1990; Martínez-García et al., 2011; Martínez-García et al., 2014) (Figure 1).
92   Given sufficient iron supply to Site U1475, the increase in nutrients would fuel local productivity
93   further enhancing glacial carbon drawdown (Martin, 1990; Martínez-García et al., 2011;
94   Martínez-García et al., 2014; Anderson et al., 2014). Indeed, northward STFZ migrations during
95   glacial periods of the past 1.4 million years are met with increased productivity at Site U1475
96   with the most significant northward frontal migrations yielding the greatest increases in biogenic
97   sediment deposition (Tangunan et al., 2021; Cartagena-Sierra et al., 2021).
98
99   While the MPT is widely regarded as an interval of global cooling, significant Southern
100   Hemisphere warming occurs during the MPT "super interglacial", MIS 31, ~1,100 ka. Prior to
101   the emergence of 100 kyr glacial-interglacial cyclicity, Southern Hemisphere insolation reaches a
102   5 Myr high, collapsing the East Antarctic Ice Sheet and delivering subtropical fauna well into the
103   modern day Subantarctic Zone (Beltran et al., 2020; McKay et al., 2012; Maiorano et al., 2009).
104   It is interesting that this destabilization of Antarctic ice sheets under relatively low atmospheric
105   CO_2 concentrations occurs immediately prior to the re-equilibration of the global climate system
106   with cooler and longer glacial intervals during the MPT. The role MIS 31 plays in the MPT
107   remains ambiguous, highlighting the need for a greater understanding of how Southern Ocean
108   processes influence and are influenced by global climate.

109
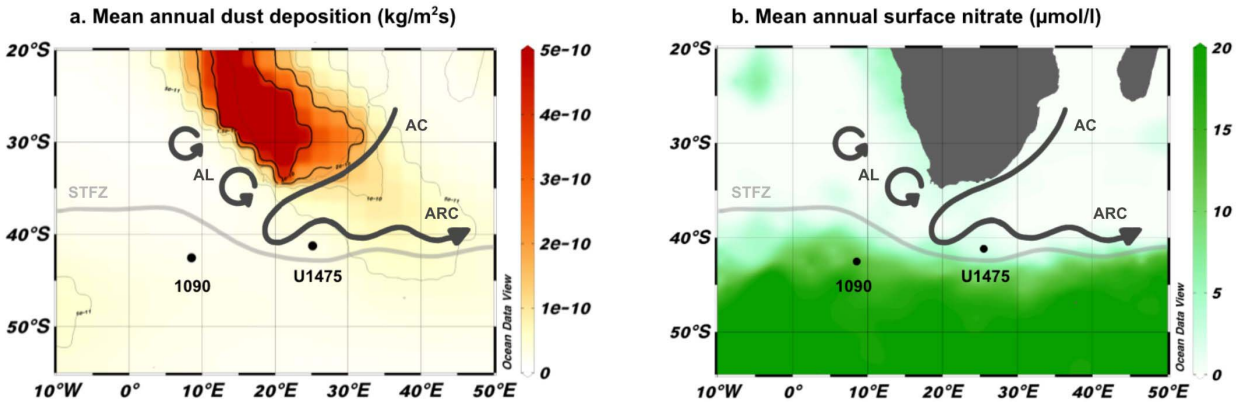
Figure 1: Map of Site U1475 and Site 1090, in the Indian-Atlantic Ocean gateway, with respect to modern a. mean annual dust deposition (kg/m^{2}s) (Li et al., 2008) and b. mean annual surface nitrate (µmol/l) (World Ocean Atlas, 2013). STFZ = Subtropical Frontal Zone; AL = Agulhas Leakage; AC = Agulhas Current; ARC = Agulhas Return Current. STFZ position from Orsi et al., (1995).

Here, we focus on the importance of frontal migrations as recorded in the nitrogen isotope values of foraminifera, in the Indian-Atlantic Ocean Gateway region across the MPT. Nitrogen isotopes provide us with a tool for documenting nutrient consumption within regions of the ocean where surface nitrate is not completely consumed and/or nutrient sources where nitrate is depleted. In the modern Southern Ocean, the nitrogen isotopic composition of nitrate, $\delta^{15}N_{NO3}$, where $\delta^{15}N$ = $[(^{15}N/^{14}N)_{sample}/(^{15}N/^{14}N)_{air}] - 1$, increases with nutrient drawdown as surface waters are advected north, yielding maximum values at the northern edge of the Southern Ocean generally, and within in the STFZ south of Africa, specifically (Figure 2a; Smart et al., 2020; Ren et al., 2009; Sigman et al., 1999). In the oligotrophic subtropical Indian Ocean, near surface $\delta^{15}N_{NO3}$ values tend to be lower than in the Southern Ocean surface, due in part to the addition of newly fixed nitrogen with a $\delta^{15}N$ of ~0‰ (Harms et al., 2019). The result is meridional increase in $\delta^{15}N_{NO3}$ values across the Southern Ocean that peaks around 42-43°S, reflecting the progressive increase in nutrient consumption, and then a decrease beyond 42°S that reflects mixing of Southern Ocean sourced nitrate with subtropically sourced nitrate in the deep mixed layer of the STFZ (Figure 2a). This trend in the $\delta^{15}N_{NO3}$ is reflected in the $\delta^{15}N$ of particulate organic nitrogen produced by phytoplankton using this nitrate pool and in turn, the particulate nitrogen is consumed by planktonic foraminifera and is the source of their $\delta^{15}N$ signal (Smart et al., 2020; Ren et al., 2009). We use the $\delta^{15}N$ values of organic matter within planktonic foraminifera shells ($\delta^{15}N_{FB}$) to study the surface nutrient dynamics in this mixing region, where the source of nitrate is the primary control on the $\delta^{15}N$ value of organic matter, yet the source $\delta^{15}N$ values are subject to change.

136
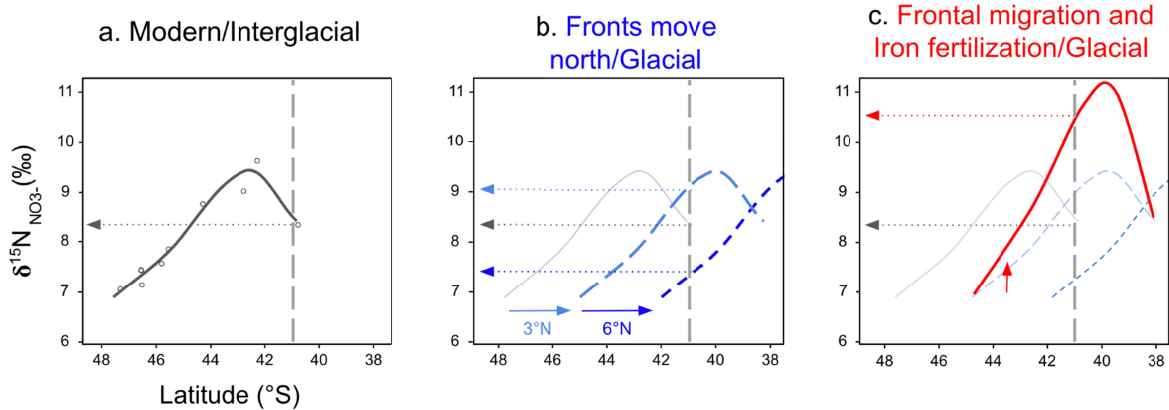
Figure 2: Schematic illustrating the $\delta^{15}N_{nitrate}$ latitudinal gradient in the modern ocean and estimated changes resulting from frontal migrations and/or iron fertilization. a. Modern $\delta^{15}N_{NO3-}$ latitudinal gradient within the Southern Ocean mixed layer (Smart et al., 2020); b. under hypothesized MPT scenarios of northward frontal migrations; c. and iron fertilization. Vertical dashed line approximates the location of Site U1475, within the present-day STFZ. Dotted arrows indicate expected $\delta^{15}N_{NO3-}$ at Site U1475 under each scenario.

To do so, we pair $\delta^{15}N_{FB}$ values with polar planktonic foraminifera species abundance, and sea surface temperatures (SST) from International Ocean Discovery Program Site U1475 (41°25′S, 25°15′E; water depth 2669 m) to provide constraints on the relative importance of physical (ocean circulation) and biological (export productivity) processes across the MPT. Site U1475 underlies the Subtropical Frontal Zone (STFZ) where warm, nutrient-poor subtropical waters meet cool, nutrient-rich polar waters at the northern edge of the Southern Ocean SAZ (Figure 1) thus it is sensitive to physical and biogeochemical changes associated with latitudinal migrations of the STFZ. We consider these additional physical water mass proxies in light of complimentary proxy records from ODP Site 1090 (42°54′S, 8°54′E; water depth 3702 m) which serves as an SAZ endmember.

We present records of $\delta^{15}N_{FB}$ from *Globigerina bulloides* ($\delta^{15}N_{FB\,G.\,bull}$) and *Globorotalia inflata* ($\delta^{15}N_{FB\,G.\,inf}$). *G. bulloides* is a cosmopolitan, opportunistic species inhabiting nutrient-rich environments, with maximum abundances south of the STFZ (Figure 3; Bé & Hutson, 1977; Haddam et al., 2016). *G. inflata* is dominant within the thermocline of transitional environments, between subtropical and polar water masses, with greatest abundance in the Indian Ocean north of Site U1475 (Figure 3; Bé & Hutson, 1977; Haddam et al., 2016). Previous studies measured $\delta^{15}N_{FB\,G.\,bull}$ to examine SAZ nutrient consumption at ODP 1090, located well within the SAZ. At U1475, within the STFZ, the $\delta^{15}N_{FB\,G.\,bull}$ may be biased toward a Southern Ocean signal and subject to potential influence from variations in SAZ nutrient demand related to Fe fertilization but also to the incursion of low latitude source nitrate into the mixing zone. $\delta^{15}N_{FB\,G.\,inf}$ values on the other hand, are more likely biased toward the Subtropical, or northern, component of the STFZ mixture. Comparison of the two records may relate to the relative position of the STFZ with respect to the core site.
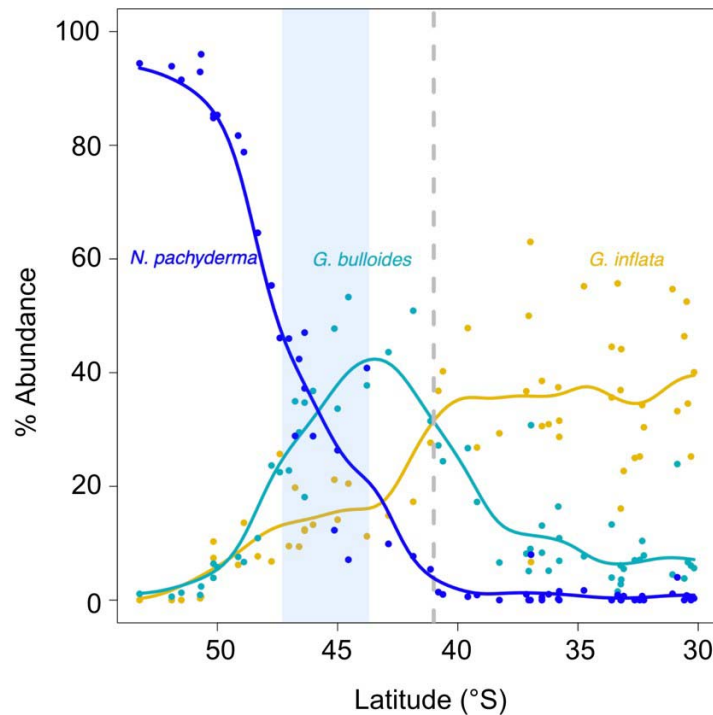
Figure 3: Modern core-top abundance of *N. pachyderma* sinistral (blue)*, G. bulloides* (teal)*, and G. inflata* (yellow) versus latitude in the region surrounding Site U1475, between 0 - 50 °E (Haddam et al., 2016). Blue shading encompasses latitudes in the modern ocean with abundances of *N. pachyderma* similar to observed glacial abundances during the MPT. Site U1475 denoted with grey dashed vertical line.

Our data demonstrate the northward migration of Southern Ocean fronts during MPT glacials. We show that the establishment of 100 kyr glacials is preceded by dramatic contraction of the Southern Ocean during the "super interglacial" Marine Isotope Stage 31, ~1,100 ka, and subsequent expansion of the Southern Ocean in the Indian-Atlantic Ocean Gateway. Expansion of the Southern Ocean appears to have occurred with an increase is biological carbon sequestration as due to enhanced biological pump efficiency in the Southern Ocean, while also altering global ocean circulation through mixing with Agulhas Leakage. Dilution of Agulhas Leakage by Southern Ocean waters may further heighten deep ocean carbon storage, increasing the residence time of surface waters and slowing overturning circulation (Starr et al., 2021).

2 Materials and Methods

2.1 Foraminifera-bound N isotopes

Individual species were identified and ~550 individuals per species were picked from the >250 μm fraction under dissecting microscope for each sample. Approximately 7 mg of picked and identified foraminifera shells were crushed between glass microscope slides and rinsed with MilliQ water. Samples were cleaned prior to $\delta^{15}N_{FB}$ measurement as follows: crushed tests were sonicated in 1.5 mL of 2% sodium hexametaphosphate, rinsed 5 times with MilliQ water and then chemically oxidized with 2 mL of an alkaline persulfate reagent (50 mL or MilliQ water, 3.25 g NaOH, 3.0 g $K_2S_2O_8$) in a pressure cooker for 60 minutes (~100 min with warm up and cool down) on a slow vent setting, followed by three MilliQ rinses, to remove external N

191 contamination (Smart et al., 2020; Ren et al., 2009). Once samples were clean, organic nitrogen
192 was released into solution by acid dissolution of the foraminiferal calcite with 75 µL of 6N
193 hydrochloric acid and converted to nitrate by the addition of 3 mL of an alkaline persulfate
194 reagent (100 mL MilliQ water, 1.6 g NaOH, 1.0 g $K_2S_2O_8$; Knapp et al., 2005; Nydahl, 1978).
195 Samples were acidified to a pH between 2-4, using ~100 µL 6N hydrochloric acid, prior to
196 measurement. Nitrate concentrations were measured by chemiluminescence on a Teledyne
197 Instruments (Model 200E) chemiluminescence NO/NOx analyzer (Braman & Hendrix, 1989).
198 $\delta^{15}N_{FB}$ samples, 10 nmol in size, were measured by bacterial conversion of nitrate to nitrous
199 oxide (Sigman et al., 2001), with measurement of the $\delta^{15}N$ of the nitrous oxide by automated
200 extraction and gas chromatography-isotope ratio mass spectrometry (Casciotti et al., 2002) on a
201 Thermo Delta V Plus IRMS. The potassium nitrate reference materials IAEA-N3 and USGS 34
202 (+4.7‰ and 1.8‰, respectively) were used to standardize results (Gonfiantini et al., 1995).
203 Note, testing of subset of 6 samples, each with full procedural triplicates, for a total of 18
204 samples, showed negligible differences in nitrogen content and $\delta^{15}N_{FB}$ values with and without a
205 reductive cleaning step, and so it was omitted here to avoid unnecessary loss of sample material.

206 Sample replicates and triplicates were analyzed when possible. Full procedural replicates were
207 analyzed for 134 sample splits, representing 66 unique samples, when enough foraminifera were
208 available for duplicate or triplicate analysis. The average standard deviation of procedural
209 replicates is 0.4‰. Full operational blanks and amino acid standards (USGS 65 glycine) were
210 measured in each batch. The average standard deviation of glycine standards measured in
211 triplicate is 0.3‰. We estimated the $\delta^{15}N$ value of the persulfate blank using a dilution series (5,
212 7.5, 10, and 20 µM of the glycine standard and the fraction of the blank in standards. We applied
213 a blank correction to each sample based on the calculated mean $\delta^{15}N$ value of all of the persulfate
214 blanks for the dataset and the fraction of the blank in the N content of each sample (see SI
215 equation S1). Data were subset to exclude N content outliers (>2 s.d. from mean and where the
216 blank was greater than 20% of the sample N content, with significantly different $\delta^{15}N$ values
217 from other replicates). The exclusion of this data does not alter statistical analyses or the findings
218 of the paper but does improve error.

219 Full propagated analytical error associated with measurement and blank correction, following
220 Higgins et al., (2009), was on average 0.6‰ (Full description in SI equation S2). Propagating the
221 errors, including not only the procedural replicates and their variance, but the relative size of the
222 blanks, the mean of the calculated blank $\delta^{15}N$ values (5± 10‰). All error bars are propagated
223 errors for each individual sample where calculated and the mean value, 0.6‰, is used where
224 procedural replicates were limited by sample availability. To verify accuracy, we measured the
225 Holocene mean $\delta^{15}N_{FB\ G.\ bull}$ value at MD02-2588, a co-located CASQ core, of 8.7 ± 0.7‰; for
226 comparison, $\delta^{15}N_{FB\ G.\ bull}$ value of the mudline sample collected at U1476 was measured to be
227 9.2 ‰ for *G. bulloides* size class 250-400 µm and 8.4‰ *bulloides* size class >400 µm (A.
228 Foreman, personal communication, 2023. The age model is based on the benthic oxygen isotope
229 stratigraphy presented by Starr et al. (2021). This age model for Site U1475 was generated with
230 12 radiocarbon dates and 33 benthic oxygen isotope tie points which were graphically aligned
231 with a probabilistic stack of 180 globally distributed benthic oxygen isotope records (Starr et al.,
232 2021).

233 2.2 Biogenic Silica

234 Approximately 200 mg of sediment was analyzed for each sample. Cleaning, chemical treatment,
235 and measurement followed protocols outlined in (Mortlock & Froelich, 1989). Samples were
236 measured with a UV Vis spectrophotometer at 812 nm wavelength. Full procedural replicates
237 were performed on 163 of the 435 samples yielding an average standard deviation of 0.2%.
238 Samples were referenced to RICCA VerSpec SiO_3^{2-} in 1% NaOH for intercomparison. Opal
239 mass accumulation rates were calculated by multiplying the fraction of opal by dry bulk density
240 and sedimentation rates from Starr et al. (2021).

241 2.3 Planktic foraminifera *Neogloboquadrina pachyderma* (sin) counts

242 Bulk planktonic foraminifera are obtained by washing ~ 10 cm³ of sediment through a 150 µm
243 sieve and drying at ~ 50 ºC for 24 h. This dried fraction is split until a total of 300-400
244 individuals remained. From this amount, we identify the relative abundance of
245 *Neogloboquadrina pachyderma* tests according to Kennett and Srinivasan (1983) and Loeblich
246 and Tappan (1988).

247 2.4 Changepoint mean analysis

248 Changepoint mean analysis was executed in R, using 'cpt.mean()' function within package
249 'changepoint' (RStudio Team, 2020) Data are averaged between replicates for each species and
250 fit to a 6 kyr evenly spaced time series using nearest neighbor interpolation, R package 'pracma',
251 function 'interp1().' Changepoint mean analysis was conducted using the following parameters:
252 test statistic = Normal; method = PELT; penalty = BIC. We consider the 0.6‰ standard
253 deviation in our interpretations, discussing short term changes greater than 1‰ and identifying
254 long term changes in the mean. Welch 2-sample t tests on all samples and replicates analyzed in
255 each section identified in the changepoint mean analysis show that each of the groups are
256 significantly different ($p<0.05$) from each other.

257 **3 Data**

258 3.1 *Neogloboquadrina pachyderma* (sin) abundance

259 Relative abundance of *N. pachyderma* (sin) varies between glacial and interglacial intervals with
260 greater abundances consistently observed in glacials. Prior to 936 ka, *N. pachyderma* (sin)
261 generally increases from 0 – 10 % in interglacials to 20 – 30 % in glacials (Figure 4). From 936 –
262 917 ka, *N. pachyderma* (sin) dominates the assemblage, reaching 60 % abundance and remains
263 above 20% throughout MIS 23 (917 – 900 ka, Figure 4). After 900 ka, *N. pachyderma* varies
264 between 45% and 0% in glacial and interglacial intervals, respectively (Figure 4).

265 3.2 Opal mass accumulation

266 Opal concentrations were overall very low, with an average value of 1.6%, at U1475. As a result,
267 opal mass accumulation rates are generally low (<0.05 mg/cm²/kyr), reaching maximum values
268 (> 0.1 mg/cm²/kyr) early in the MPT, ~1,100 ka (Figure 5). After this initial peak, opal mass
269 accumulation declines slightly, remaining near ~ 0.06 mg/cm²/kyr until ~800 ka, after which
270 opal accumulation remains largely below 0.05 mg/cm²/kyr (Figure 5).

271   3.3 Foraminifera-bound N isotopes

272   Across the MPT, $\delta^{15}N_{FB\ G.\ bull}$ values are generally higher than $\delta^{15}N_{FB\ G.\ inf}$ values (Figure 4).
273   While $\delta^{15}N_{FB\ G.\ bull}$ values are less variable and tend to be highest in the early MPT, prior to 1,100
274   ka, $\delta^{15}N_{FB\ G.\ inf}$ values are less variable and tend to be highest during the mid-late MPT, after ~790
275   ka. Both species exhibit minimum $\delta^{15}N_{FB}$ values during the "super interglacial" Marine Isotope
276   Stage (MIS) 31, ~1,070 ka.

DRAFT

277
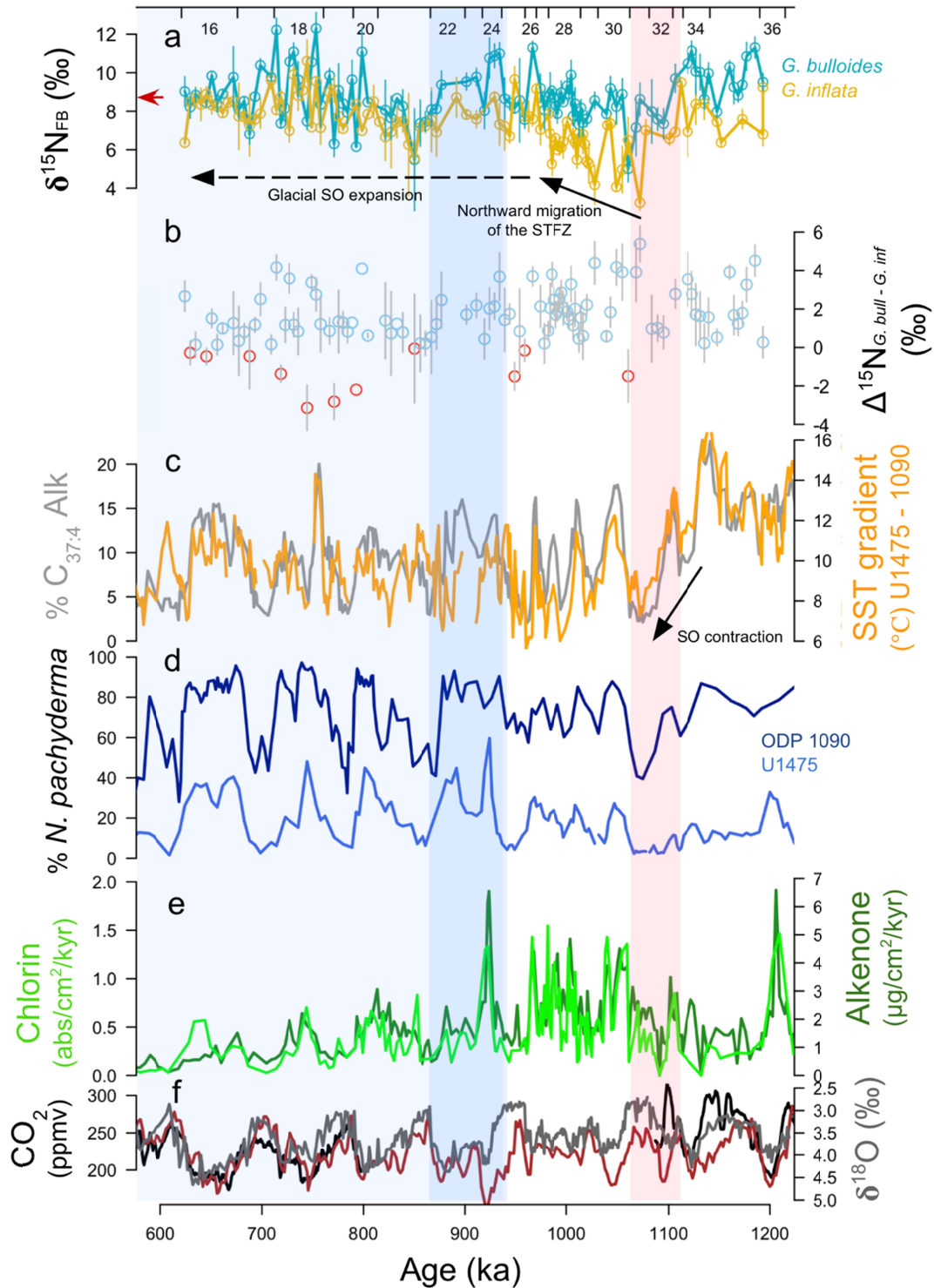
Figure 4: Biogeochemical records measured from Sites U1475 and ODP 1090. a. $\delta^{15}N_{FB}$ of *G. bulloides* and *G. Inflata*, vertical lines indicate propagated error for each sample. The average Holocene *G. bulloides* value from a co-located core (MD0202588) are indicated by the red arrow on the y axis; b. $\Delta\delta^{15}N_{FB}$, *G. bulloides* – *G. inflata*, where blue circles indicate positive and red indicate negative values, gray bars span vertical lines span ± 1 standard deviation; c. U^{k}_{37}' SST gradient between Site U1475 (Cartagena-Sierra et al., 2021) and ODP 1090 (Martínez-García et al., 2010) and percent $C_{37:4}$ alkenones at ODP 1090 (grey, Martínez-García et al., 2010); d. Percent abundance of

284   polar species *N. pachyderma* at Site U1475 and Site 1090 (Becquey & Gersonde, 2002); e. Alkenone and chlorin
285   mass accumulation rates (Cartagena-Sierra et al., 2021) ($\mu g/cm^2/kyr$ and abs/cm^2/kyr; dark and light green
286   respectively). U1475 age model from Starr et al. (2021); f. Atmospheric CO_2 from EPICA Dome C (black, Bereiter
287   et al., 2015), $\delta^{11}B$-based reconstruction (black, Hönisch et al., 2009), and $\delta^{13}C_b$ models (red, Lisiecki, 2010); Site
288   U1475 benthic $\delta^{18}O$ *Cibicidoides wuellerstorfi* (gray, Starr et al., 2021). Marine Isotope Stages are noted along the
289   top axis. Light blue shading indicates 100 kyr world, dark blue shading indicates "900 kyr" event, red shading
290   indicates "super interglacial".
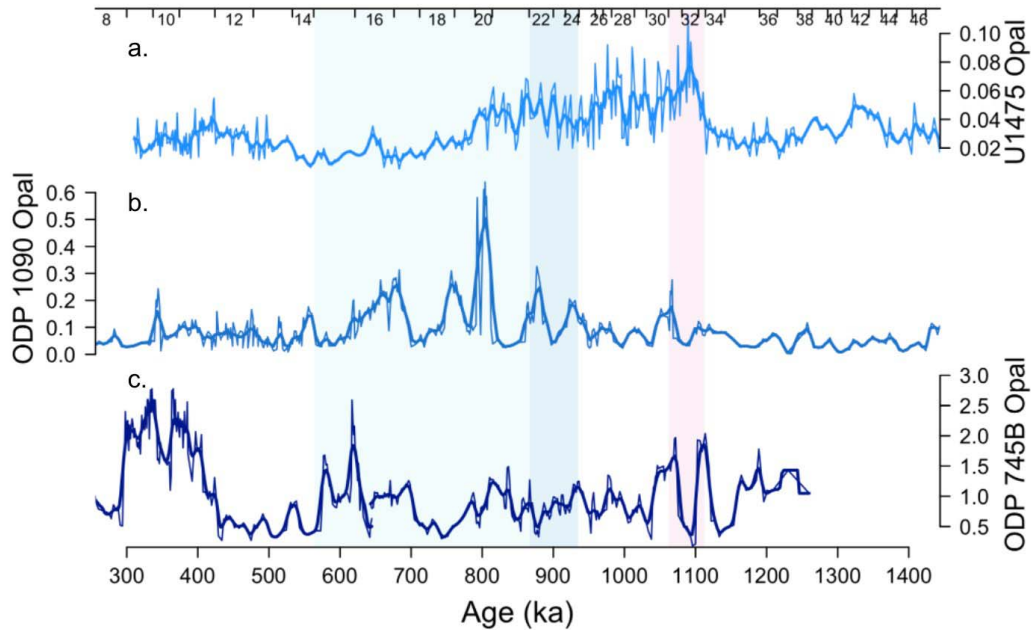
291

292   Figure 5: Opal mass accumulation rates ($mg/cm^2/kyr$) from the a. Subtropical frontal zone, IODP Site U1475; b.
293   Subantarctic Zone, ODP Site 1090 (Diekmann & Kuhn, 2002); c. Antarctic Zone, ODP Site 745B (Kaiser et al.,
294   2021; Billups et al., 2018) showing a southward shift in the relative, site specific, magnitude of biogenic opal
295   deposition within the Southern Ocean around the MPT. Bold lines show a 10 kyr kernel smoothing. Marine Isotope
296   Stages are noted along the top axis and red/blue shading corresponds to shading in Figure 4.
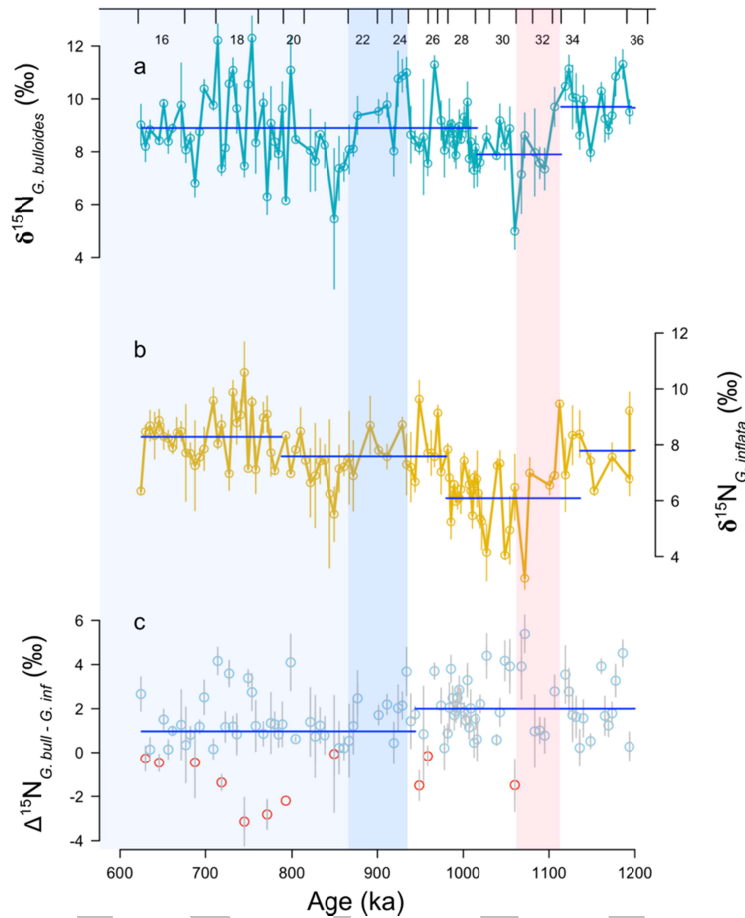
Figure 6: Results from changepoint mean analysis of a. $\delta^{15}N_{FB\ G.\ bulloides}$; b. $\delta^{15}N_{FB\ G.\ inflata}$; and c. $\Delta\delta^{15}N_{FB}$, *G. bulloides* – *G. inflata*, where blue circles indicate positive and red indicate negative values. Blue lines indicate mean $\delta^{15}N_{FB}$ of a statistically similar interval, with significant changes in the mean marked by a change in the y position, or mean $\delta^{15}N_{FB}$ value, of the line. Vertical bars span ± 1 standard deviation. Marine Isotope Stages are noted along the top axis and red/blue shading corresponds to shading in Figure 4.

4 Discussion

4.1 Long timescale changes in $\delta^{15}N$ above the Agulhas Plateau

The long timescale variation in $\delta^{15}N$, with lower $\delta^{15}N_{FB\ G.\ bull}$ and $\delta^{15}N_{FB\ G.\ inf}$ values around 1,100 ka, with a minimum during MIS 31-33, followed by a return to a more elevated mean values by 900ka, is mirrored in the SST gradient, Uk'$_{37:4}$, and *N. pachyderma* abundance records suggesting a strong link between surface ocean nutrient dynamics and the climate driven position of the Subtropical Front. Changepoint mean analysis reveals two significant timepoints in each species' $\delta^{15}N_{FB}$ record (Figure 6) that highlight the long term trends. From 1,200 – 1,114 ka the $\delta^{15}N_{FB\ G.\ bull}$ values vary around a mean of 9.7‰, a significant changepoint occurs at 1,114 ka when mean $\delta^{15}N_{FB\ G.\ bull}$ is reduced to 7.9‰ until 1,016 ka (Figure 6). After 1,016 ka $\delta^{15}N_{FB\ G.\ bull}$ values vary around a mean of ~ 8.9 ‰ (Figure 6). In contrast, $\delta^{15}N_{FB\ G.\ inf}$ values vary around a mean of 7.8‰ prior to 1,136 ka, from 1,136 – 980 ka mean $\delta^{15}N_{FB\ G.\ inf}$ is 6.1 ‰, from 980 – 788 ka mean $\delta^{15}N_{FB\ G.\ inf}$ is 7.6 ‰ and after 788 ka mean $\delta^{15}N_{FB\ G.\ inf}$ rises to 8.3 ‰ (Figure 6). The potential controls on the $\delta^{15}N$ records are: 1) variations in the relative contribution from

318   Subtropical versus Subpolar water masses, 2) variation in the relative contributions from locally
319   grown versus advected foraminifera, 3) variations in the $\delta^{15}N$ values of the Subtropical source
320   water, 4) variations in the $\delta^{15}N$ value of the Subpolar source, and 5) local variations in the
321   relative utilization of nitrate. To some degree, all of these factors are likely to contribute to this
322   record.

323   Subtropical and Subpolar waters converge in the STFZ and their relative contributions likely
324   vary over time with climate. The early MPT, prior to ~1,140 ka, is marked by ice sheet
325   expansion, cool SST's, and elevated *N. pachyderma* (sin) abundance at Site 1090 (McKay et al.,
326   2012; Martínez-García et al., 2010; Beltran et al., 2020) (Figure 4; Figure S2). Yet, warm SST's
327   and low *N. pachyderma* (sin) abundance at Site U1475 prior to 1,140 ka indicates the STFZ was
328   located south of Site U1475. Records of Agulhas Leakage indicate transfer of water from the
329   Indian into the Atlantic Ocean, consistent with this inference (Caley et al., 2012). The early MPT
330   interval of ice-sheet expansion is terminated by the "super interglacial" of MIS 31 (~1,070 ka,
331   McKay et al., 2012; Beltran et al., 2020) and a dramatic southward shift of the STFZ.
332
333   Southern Hemisphere insolation reaches a 5 Myr high during MIS 31, ~1,070 ka, resulting in
334   dramatic Antarctic ice loss and Southern Hemisphere warming (Beltran et al., 2020; McKay et
335   al., 2012; Maiorano et al., 2009) (Figure S2). Southward displacement of the STFZ is evidenced
336   by reduced presence of polar species *N. pachyderma* (sin) at Site 1090, a sharp reduction in the
337   SST gradient between Sites U1475 and 1090, reduced % $C_{37:4}$ at Site 1090 (Figure 4), and by
338   increased presence of Subtropical Convergence/Agulhas Current nannofossil assemblages at Site
339   1090 from MIS 33-31 (1,114 – 1,062 ka, Maiorano et al., 2009). The reduced SST gradient is
340   largely driven by warming at Site 1090 (Figure S2). This marks a sustained reduction in the SST
341   gradient relative to values observed prior to MIS 33, ~1,110 ka (Figure 4). Interestingly, biogenic
342   opal deposition at Site U1475 is highest during the "super interglacial", despite evidence for
343   significant contraction of the Southern Ocean (Figure 5). The STFZ is associated with a
344   deepening of the mixed layer depth and may indicate localized enhanced nutrient supply and
345   consequent production related to this deep mixing (Monterey & Levitus, 1997).
346
347   The extreme southward shift in the STFZ is contemporaneous with significant reductions in the
348    $\delta^{15}N_{FB}$ values. This interval is highlighted as a significant changepoint between MIS 33 – 31
349   (Figure 6). Low $\delta^{15}N_{FB}$ values are consistent with a greater contribution of nitrogen from the
350   Subtropics, either through the advection of Subtropically sourced nitrate with low $\delta^{15}N$ values to
351   the core site, resulting in low $\delta^{15}N$ PON production and consumption by local foraminifera, or
352   the advection of more foraminifera from the Subtropics to the core site. Model results reveal the
353   Agulhas Current is capable of carrying plankton nearly 1,000 km over a typical 30 day lifespan
354   (van Sebille et al., 2015) and so at least some contribution from advected foraminifera is likely.
355   While both potential contributions of nitrogen point to a more important Subtropical source
356   during MIS 31 - 33, the need to make a distinction comes into play if one wants to assign an
357   endmember $\delta^{15}N$ value to the Subtropical nitrogen or use the relative proportion of Subpolar
358   versus subtropical planktic foraminiferal abundances to weight these endmember values. The
359   possibility of locally grown versus imported foraminifera muddies these ideas further.

360   The need to understand the endmember $\delta^{15}N$ values is highlighted by the fact that the $\delta^{15}N_{FB}$
361   values observed during MIS 31-33 are exceptionally low relative to the rest of the record, and
362   also relative to expectations based on to modern southern Indian Ocean values (Harms et al.,
363   2016; Marshall et al., 2023). These low $\delta^{15}N_{FB}$ values require not only an increase in
364   contributions of Subtropical nitrogen but also a decrease in the $\delta^{15}N$ of the nitrogen sourced to
365   the STFZ. A decrease in the $\delta^{15}N$ of the Subtropically sourced nitrogen can be explained by
366   increases in nitrogen fixation derived nitrogen in the Agulhas Current region. Today N fixation,
367   which brings in N with a $\delta^{15}N$ value of ~-1‰, occurs in the source regions to and along the
368   flowpath of the Agulhas Current (Dupuy et al., 2016; Kolasinski et al., 2012; Marshall et al.,
369   2023). In addition, throughout interglacial periods of the last 800 kyr, increased denitrification
370   has been documented in the Arabian Sea (Kim et al., 2018) thus it is probable that during this
371   "super interglacial" we may see an exceptional response in N fixation to balance N losses from
372   denitrification. Our data pose an interesting question as to whether a significant change in the
373   magnitude of Indian Ocean denitrification and N fixation occurs at this time. N isotope data from
374   upstream locations would be useful in confirming these changes.

375   At the same time that Subpolar nitrate likely became less important at U1475, the $\delta^{15}N$ of the
376   Subpolar sourced nitrogen, either as nitrate or in advected Subpolar foraminifera, may also have
377   decreased. Prior to the super-interglacial warming, we observe high $\delta^{15}N_{FB}$ values particularly in
378   *G. bulloides* coincident with the SST gradient and Site 1090 %$C_{37:4}$ maxima and Southern
379   Hemisphere insolation minimum (Figure 4, Figure S2). Part of the elevation in $\delta^{15}N$ values may
380   be due to the northward shifted Southern Ocean fronts, documented by the Site 1090 *N.*
381   *pachyderma* (sin) and SST gradient data, and the associated relative contribution of Subpolar
382   nitrogen at U1475. Yet, the observed $\delta^{15}N_{FB\ G.bull}$ values (11‰) exceed the modern latitudinal
383      $\delta^{15}N_{NO3-}$ maxima expected near the STFZ (9.5‰) and are ~3‰ greater than the expected $\delta^{15}N_{FB}$
384      $_{G.bull}$ (Figure S1). This implies an increase in the $\delta^{15}N$ value of the source nitrogen. We infer that
385   relative nutrient consumption was elevating the $\delta^{15}N$ value of nitrate (Figure 1, Figure 4). This
386   could be due to a local increase in nutrient consumption or a regional increase and the advection
387   of this signal northwards from the SAZ. Without an increase in productivity at Sites 1090 or
388   U1475, enhanced nutrient consumption requires an overall reduction in nutrient supply prior to
389   1,110 ka. Indeed, ice sheet expansion may have contributed to weaker overturning within the
390   Southern Ocean that limited nutrient supply and increased relative nitrate consumption
391   regionally (Starr et al., 2021; Ferrari et al., 2014). After 1,110 ka, Southern Ocean warming
392   during "super interglacial" MIS 31 coincides with a significant reduction in $\delta^{15}N_{FB}$ values and a
393   decrease in the $\delta^{15}N$ of nitrogen from both the Subtropical and Subpolar sources is likely.

394   4.3 Transitional expansion of the glacial Southern Ocean prior to the 100 kyr glacial periods

395   The Southern Ocean experienced significant geographic expansion during glacial stages
396   following 900 ka. *N. pachyderma* (sin) abundances indicate that the glacial expansions began
397   gradually after MIS 31, (~1,060 ka), increasing in each glacial period until MIS 24 (~930 ka)
398   when the STFZ achieved its northernmost position. At ~930 ka, *N. pachyderma* (sin)
399   abundances exceeded 60% at Site U1475, which, based on *N. pachyderma* (sin) surface sediment
400   distributions suggest an 8 degree northward migration in the average latitude of STFZ (Figures 3
401   & 4). Higher abundances of *N. pachyderma* (sin) in 100 kyr glacials, after ~920 ka, indicates
402   increased influence of polar waters near Site U1475. The northward shift in polar waters is

403   supported by the relative proportion of the cold, %$C_{37:4}$ alkenones at the nearby SAZ ODP Site
404   1090 (Martínez-García et al., 2010) (Figure 4) and abundance of ice-rafted debris (IRD) at Site
405   U1475 (Figure S2, Starr et al., 2021). This northward migration of the STFZ would deliver
406   nitrate rich waters further north, fueling the enhanced export productivity recorded by chlorin
407   and alkenone accumulation from ~1,010 – 920 ka (Figure 4). The relatively high $\delta^{15}N$ of this
408   southern sourced nitrate is evident in the progressive increase in $\delta^{15}N_{FB}$ values (Figure 6).

409   4.4 An expanded glacial Southern Ocean amplifies Fe fertilization in the 100 kyr world

410   The $\delta^{15}N_{FB}$ values at Site U1475 after 900 ka likely reflect the increased or dominant presence of
411   the Southern Ocean waters that, because they are nutrient bearing, also record the nutrient
412   consumption signal attributable to enhanced iron delivery (Martinez-Garcia et al., 2011). The
413   STFZ maintains a northward position, as evidenced by *N. pachyderma* (sin) abundance and IRD
414   deposition, from ~930 – 860 ka and, based on the relatively high $\delta^{15}N_{FB}$ values, an extended
415   period of enhanced nutrient drawdown (Figure 4, Figure S2). Similar to the interval prior to the
416   super-interglacial, expansion of the Southern Ocean alone cannot fully explain the glacial $\delta^{15}N_{FB}$
417   values recorded at Site U1475. A slowdown in overturning circulation is recorded by the
418   accumulation of respired organic carbon in the deep ocean (Farmer et al., 2017; Lear et al.,
419   2016). Expanded Southern Ocean sea ice and enhanced stratification at ~900 ka would have
420   limited the supply of nutrients and carbon to the surface contributing to the elevated $\delta^{15}N_{FB}$
421   values observed across this interval (Hasenfratz et al., 2019). This interplay between biological
422   drawdown and physical trapping of carbon occurs across the "900 ka event", prior to the
423   establishment of 100 kyr cyclicity in deep ocean biogeochemical records (Ford & Chalk; 2020;
424   Starr et al., 2021; Farmer et al., 2019; Pena & Goldstein, 2014).

425   In glacial intervals following 900 ka, the supply of southern sourced nutrients to Site U1475
426   supported modest increases in biological productivity that are reflected in slightly elevated
427   biogenic sediment accumulation rates while elevated glacial $\delta^{15}N_{FB}$ values suggest continued
428   greater demand for nutrients and reduced Subtropical nitrogen contributions (Figure S3). The
429   expectation for a slight northward shift in the fronts without any change in the degree of nutrient
430   consumption regionally is an increase in the $\delta^{15}N_{NO3-}$ value (due to reduced contribution of low
431     $\delta^{15}N$ subtropical NO_3^-). While a larger northward shift in the latitude of the STFZ, as predicted in
432   MPT glacials by *N. pachyderma* (sin) abundances (Figure 2b), would result in lower $\delta^{15}N_{NO3-}$,
433   unless a significant increase in nutrient demand relative to availability accompanies these frontal
434   migrations. Glacial *N. pachyderma* (sin) abundances indicate a 3 - 6 degree northward migration
435   of the STFZ, again suggesting that the $\delta^{15}N_{FB}$ enrichments, on average 3‰ between average
436   interglacial minima and glacial maxima cannot be explained without enhanced nutrient
437   consumption (Figure 2 & 4) (Haddam et al., 2016). We use $\delta^{15}N_{FB\ G.\ bull}$ values to estimate a
438   change in Southern Ocean nutrient consumption on glacial-interglacial timescales during the
439   MPT, assuming the $\delta^{15}N_{FB\ G.\ bull}$ signal after MIS 31 dominantly reflects changes in relative
440   consumption. We use measurements from *G. bulloides* to more easily relate to estimates from
441   Site 1090 spanning the last glacial period.

442   Assuming no net change in supplied nitrate concentration or isotopic composition at 41°S, we
443   apply a Rayleigh model to estimate changes in the degree of summer nitrate consumption
444   associated with a 3‰ increase in $\delta^{15}N_{FB\ G.\ bull}$ (Altabet & Francois, 1994; Fripiat et al., 2019)

445 (Figure S1b). We calculate the integrated phytoplankton biomass N assimilated during summer
446 nitrate drawdown using the "integrated product" equation, where $\delta^{15}N_{integ.prod.} = \delta^{15}N_{initial} + e *$
447 $([NO_3\text{-}]/([NO_3\text{-}]_{initial} - [NO_3\text{-}])) * \ln([NO_3\text{-}]/[NO_3\text{-}]_{initial})$ and $[NO_3^-]_{initial}$ and $\delta^{15}N_{initial}$ are the nitrate
448 concentration and $\delta^{15}N_{NO3\text{-}}$ in the water supplied to the summertime surface mixed layer prior to
449 nutrient drawdown, $[NO_3^-]$ is the nitrate concentration after the nutrient drawdown period, and e
450 is the isotope effect of nitrate assimilation. Here we assume an isotope effect of 6.5‰, consistent
451 with estimates for SAZ surface layer nitrate drawdown (DiFiore et al., 2010) (Figure S1).
452 $\delta^{15}N_{initial}$ and $[NO_3^-]_{initial}$ are taken from water column measurements beneath the mixed layer at
453 41°S, 10.1‰ and 8.4 µM (Smart et al., 2020). Using these parameters, the $\delta^{15}N$ of the
454 photosynthetic biomass produced is estimated to be 4.4‰, and $\delta^{15}N_{FB\ G.\ bull}$ is expected to be
455 7.5‰, based on a 3.1‰ trophic offset (Smart et al., 2020) (Figure S1b). These estimates are
456 slightly lower than average interglacial data (8.7‰) and Holocene data (8.7‰) from Site U1475.
457 Assuming similar conditions to modern, we use the integrated product estimation to link changes
458 in $\delta^{15}N_{FB}$ values to nitrate consumption. Under these conditions, mean glacial maxima $\delta^{15}N_{FB}$
459 values of 10.2‰ and MIS 24 values of 10‰ are consistent with surface ocean nitrate
460 concentrations below 2.2 µM (Figure S1b). Surface ocean nitrate concentrations indicate near
461 complete nutrient consumption in glacial intervals with potentially >70% of surface ocean
462 nutrients at Site U1475 drawn down. Between peak interglacial and glacial conditions, we
463 estimate that relative nutrient consumption increased from 16% up to 70%, consistent with
464 nutrient drawdown exceeding the increase in nutrient supply (Figure 4; Figure S1b). This
465 estimate does not reflect the real nuances discussed above associated with the potential variations
466 in the source $\delta^{15}N$ values or relative contributions of advected versus locally grown foraminifera.

467 If glacial mixing of SAZ and subtropical water remains similar amongst glacial periods
468 following 900 ka, as the consistent glacial abundances of *N. pachyderma* (sin) imply,
469 maintaining similar mean $\delta^{15}N_{FB}$ values with smaller magnitude increases in biogenic sediment
470 accumulation requires that nutrient supply decreased. This can be explained by a wholesale
471 slowdown in nutrient supply or a shift in the locus of nutrient consumption and the advection of
472 the nitrogen isotopic signature of enhanced consumption northwards. Intermittent increases in
473 biogenic opal accumulation occur in the SAZ after 900 ka and after 400 ka in the AZ perhaps
474 suggesting a progressive southward shift in productivity (Figure 5) (Diekmann & Kuhn, 2002;
475 Billups et al., 2018; Kaiser et al., 2021). Our observation supports a more polar Southern Ocean
476 driver, whether biological or physical, of carbon sequestration during late MPT glacials.

477 Species specific differences in $\delta^{15}N_{FB}$

478 In addition to the large scale shifts in the mean $\delta^{15}N_{FB}$ seen in both the *G. bulloides* and *G.*
479 *inflata* datasets, differences between the two records and the differences between species also
480 vary with the inferred latitudinal migrations of the STFZ (Figure 6). A significant changepoint
481 occurs in the record of the $\delta^{15}N_{FB}$ difference between the species ($\Delta\delta^{15}N_{FB} = \delta^{15}N_{FB\ G.\ bull}$ -
482 $\delta^{15}N_{FB\ G.\ inf}$), with decrease in the $\Delta\delta^{15}N_{FB}$ across the MPT with a >1 ‰ reduction in the mean
483 after 933 ka reducing $\Delta\delta^{15}N_{FB}$ value from ~ 2.5 ‰ to 1.1 ‰ (Figure 6). The consistent offset
484 between $\delta^{15}N_{FB\ G.\ bull}$ and $\delta^{15}N_{FB\ G.\ inf}$ values, in which $\delta^{15}N_{FB\ G.\ bull}$ values are higher, is counter to
485 modern observations collected from net tows and sediment traps in Indian-Atlantic Ocean
486 Gateway (Smart et al., 2020) (Figures 4 & 6). In the modern ocean, *G. inflata* records a higher

487 $\delta^{15}N_{FB}$ value than *G. bulloides* captured in the same net tow. This is attributable to its preference
488 for a deeper habitat, possibly related to the consumption of a more degraded PON pool for
489 nutrition (Smart et al., 2020). If depth was the primary control on differences between $\delta^{15}N_{FB\,G.}$
490 $_{bull}$ and $\delta^{15}N_{FB\,G.\,inf}$ values in the Site U1475 record we would expect to see consistently higher
491 $\delta^{15}N_{FB\,G.\,inf}$ values. Since we do not, we explore the possibility that the differences relate to
492 seasonal export events and/or foraminiferal habitat preferences and advection.

493 Within the Southern Ocean, *G. bulloides* exhibits two export episodes to the sediments each year,
494 once in spring and again in fall (Kretschmer et al., 2018; King & Howard, 2005; Jonkers &
495 Kučera, 2015). In contrast, *G. inflata* export flux peaks once, in spring (Jonkers & Kučera, 2015;
496 Bé & Hutson, 1977). Thus, seasonal biases may yield higher $\delta^{15}N_{FB}$ values in *G. bulloides* if
497 nutrients are more depleted in fall than in spring. This is not entirely consistent with modern
498 observations from this region where late summer $\delta^{15}N_{NO3^-}$ values are reduced by mixing with low
499 $\delta^{15}N_{NO3^-}$ subtropical waters indicating that seasonality does not provide a robust explanation
500 (Smart et al., 2020). Further, as climate cools *G. bulloides* is expected to bias its export towards
501 warmer seasons while *G. inflata* would be less affected; this could further reduce the $\delta^{15}N_{FB\,G.\,bull}$
502 relative to $\delta^{15}N_{FB\,G.\,inf}$ (Jonkers & Kučera, 2015).

503 However, planktic foraminifera are also subject to advection into this mixing zone. North of Site
504 U1475, *G. inflata* is present in greater abundance than *G. bulloides*, but to the south *G. bulloides*
505 abundance exceeds *G. inflata* (Figure 2). If we view the STFZ as a convergence zone of
506 subtropical and subpolar planktic foraminifera, we can explain the observed $\delta^{15}N_{FB}$ values of *G.*
507 *bulloides* and *G. inflata* more easily. On average, the *G. inflata* measured at Site U1475 are
508 biased towards recording the subtropical signature of the Agulhas Current, where at least some
509 fraction of the *G. inflata* in the sediment must have integrated the low $\delta^{15}N$ PON signal into their
510 shell in the Subtropics to be ultimately deposited along the STFZ. Similarly, Ekman transport of
511 Southern Ocean surface water would deliver *G. bulloides* grown in the SAZ to Site U1475. Some
512 contribution of advected *G. bulloides* from the south and *G. inflata* from the north best explains
513 the higher $\delta^{15}N$ values of *G. bulloides* compared to *G. inflata*. The difference between $\delta^{15}N_{FB}$
514 values of *G. bulloides* and *G. inflata* is smallest during "super interglacial" MIS 31 and after 933
515 ka, with the most similar values occurring when *N. pachyderma* (sin) abundances indicate
516 considerable latitudinal migrations of the STFZ leading to greater similarity in $\delta^{15}N$ values of the
517 sources to both species (Figure 4). To put it another way, when the front is furthest from U1475,
518 either to the north or south, foraminifera $\delta^{15}N$ values reflect a shared local Subantarctic or
519 Subtropical food source, whereas when the mixing zone is close to overhead, foraminifera are
520 advected from different regions.

521 Both species exhibit significant changes in their mean $\delta^{15}N_{FB}$ values associated with these
522 significant frontal migrations, however, *G. inflata*'s changes lag relative to *G. bulloides*,
523 suggesting that $\delta^{15}N_{FB\,G.\,bull}$ is a sensitive and early indicator of southward migrations of the
524 STFZ, with reductions in $\delta^{15}N_{FB\,G.\,bull}$ occurring as early as MIS 33 (Figure 6). After MIS 31, the
525 $\delta^{15}N_{FB}$ values of both species significantly increase (Figure 6). The earlier increase in mean
526 values of *G. bulloides* is consistent with a northward migration of the STFZ and expansion of the
527 southern sourced $\delta^{15}N$ signal (Figure 6).

528

5 Conclusions

Across the MPT, $\delta^{15}N_{FB}$ records from Site U1475 change in tandem with STFZ migrations. The largest change in $\delta^{15}N_{FB}$ values results from Southern Ocean contraction and dominance of a low $\delta^{15}N$ subtropical nutrient signal during the "super interglacial" MIS 31, ~1080 ka. Glacial intervals prior to MIS 31 were cold in the Subantarctic but still relatively warm in the STFZ with the front located firmly south of the Agulhas Plateau. Glacials following MIS 31 are characterized by northward migrations of the STFZ in the Indian-Atlantic Ocean Gateway with potential for >6 degree northward migration of the STFZ during MIS 24, 936 – 917 ka and glacials after 900 ka are characterized by greater abundance of polar foraminifera and a reduced SST gradient between Sites U1475 and 1090, consistent with a more northern STFZ. More similar $\delta^{15}N_{FB}$ values between *G. bulloides* and *G. inflata* after MIS 24 also support a northern expansion of Southern Ocean nitrate and reduced influence of low $\delta^{15}N$ subtropical nitrate at Site U1475 after 900 ka. These data suggest that not only cooling of the Southern Ocean but also its expansion is necessary to expand the length of ice ages across the MPT.

The increases in $\delta^{15}N_{FB}$ associated with northward migrations of the front are likely amplified by changes in nutrient consumption. Despite higher supply of nitrate and reduced subtropical water contribution in MPT glacials, it seems that nutrient consumption increased, likely related to iron fertilization. Glacial expansion of the Southern Ocean has the potential to enlarge the total nutrient replete area and it also may facilitate iron fertilization by bringing these nutrient rich waters closer to Southern Hemisphere iron sources which would otherwise be unavailable. In this region, a >6 degree northward migration of the STFZ would deliver nitrate bearing surface waters into latitudes receiving twice as much annual dust deposition, linking physical and biological carbon feedbacks (Figure 1; Jaccard et al., 2016). A complimentary iron accumulation record from Site U1475 would allow us to determine whether northward expansion of the STFZ, and associated proximity to South African iron sources, could stimulate additional nutrient drawdown. A $\delta^{15}N_{FB}$ record from a site north of Site U1475 would allow us to account for any reduction of the $\delta^{15}N_{FB}$ values at Site U1475 due to mixing with subtropical water or changes in the proportion of fixation derived N.

A northward shift in the position of the STFZ in this region would alter physical ocean circulation, increasing the residence time of this carbon in the deep ocean. We hope that future work to generate nutrient consumption and Fe records will clarify the extent to which Fe fertilization further enhances C sequestration. This interplay between physical and biological feedbacks in the Indian-Atlantic Ocean Gateway may play a critical role in increasing deep ocean carbon storage and lengthening glacial cycles during the MPT.

Acknowledgments

Authors contributions: B. A. M., R. S. R., A. C-S. and M. A. B. conceived the project and contributed to the writing. B. A. M. and R. S. R. collected and analyzed the foraminifera bound N isotope data. T. P.d S. and D. L. collected and analyzed the foraminiferal assemblage data and

569 contributed to the interpretation and writing. I. A. H., A. S., and A. C-S. contributed to the data
570 interpretation and writing.

571 **Competing interests:** The authors have no known competing interests at this time.
572 **Open Research:**
573 All new data presented in this paper are archived at Pangaea (Marcks et al., 2022a), (Marcks et
574 al., 2022b), and (Marcks et al., 2022c).
575
576

577 **References:**

578

579 Altabet, M. A., & Francois, R. (1994). Sedimentary nitrogen isotopic ratio as a recorder for
580 surface ocean nitrate utilization. *Global Biogeochemical Cycles*, *8*(1), 103–116.
581 https://doi.org/10.1029/93GB03396

582

583 Anderson, R. F., Barker, S., Fleisher, M., Gersonde, R., Goldstein, S. L., Kuhn, G., Mortyn, P.
584 G., Pahnke, K., & Sachs, J. P. (2014). Biological response to millennial variability of dust and
585 nutrient supply in the Subantarctic South Atlantic Ocean. *Philosophical Transactions of the
586 Royal Society A: Mathematical, Physical and Engineering Sciences*, *372*(2019), 20130054.
587 https://doi.org/10.1098/rsta.2013.0054

588

589 Antell, G. S., Fenton, I. S., Valdes, P. J., & Saupe, E. E. (2021). Thermal niches of planktonic
590 foraminifera are static throughout glacial–interglacial climate change. *Proceedings of the
591 National Academy of Sciences*, *118*(18), e2017105118. https://doi.org/10.1073/pnas.2017105118

592

593 Bard, E., & Rickaby, R. E. M. (2009). Migration of the subtropical front as a modulator of glacial
594 climate. *Nature*, *460*, 380-383. https://doi.org/10.1038/nature08189

595

596 Bé, A. W. H., Hutson, W. H., & Be, A. W. H. (1977). Ecology of Planktonic Foraminifera and
597 Biogeographic Patterns of Life and Fossil Assemblages in the Indian Ocean. *Micropaleontology*,
598 *23*(4), 369–369. https://doi.org/10.2307/1485406

599

600 Beal, L. M., De Ruijter, W. P. M., Biastoch, A., Zahn, R., Cronin, M., Hermes, J., Lutjeharms, J.,
601 Quartly, G., Tozuka, T., Baker-Yeboah, S., Bornman, T., Cipollini, P., Dijkstra, H., Hall, I., Park,
602 W., Peeters, F., Penven, P., Ridderinkhof, H., & Zinke, J. (2011). On the role of the Agulhas
603 system in ocean circulation and climate. *Nature*, *472*(7344), 429–436.
604 https://doi.org/10.1038/nature09983

605

606 Becquey, S., & Gersonde, R. (2002). Past hydrographic and climatic changes in the Subantarctic
607 Zone of the South Atlantic – The Pleistocene record from ODP Site 1090. *Palaeogeography,
608 Palaeoclimatology, Palaeoecology*, *182*(3–4), 221–239. https://doi.org/10.1016/S0031-
609 0182(01)00497-7

610

611 Beltran, C., Golledge, N. R., Christian, O., Kowalewski, D. E., Marie-Alexandrine, S., Hageman,
612 K. J., Robert, S., Wilson, G. S., & François, M. (2020). Southern Ocean temperature records and

613   ice-sheet models demonstrate rapid Antarctic ice sheet retreat under low atmospheric CO2

614   during Marine Isotope Stage 31. *Quaternary Science Reviews*, *228*.

615   https://doi.org/10.1016/j.quascirev.2019.106069

616

617   Bereiter, B., Eggleston, S., Schmitt, J., Nehrbass-Ahles, C., Stocker, T. F., Fischer, H., Kipfstuhl,

618   S., & Chappellaz, J. (2015). Revision of the EPICA Dome C CO $_2$ record from 800 to 600 kyr

619   before present: Analytical bias in the EDC CO2 record. *Geophysical Research Letters*, *42*(2),

620   542–549. https://doi.org/10.1002/2014GL061957

621

622   Billups, K., York, K., & Bradtmiller, L. I. (2018). Water Column Stratification in the Antarctic

623   Zone of the Southern Ocean During the Mid-Pleistocene Climate Transition. *Paleoceanography*

624   *and Paleoclimatology*, *33*(5), 432–442. https://doi.org/10.1029/2018PA003327

625

626   Braman RS, Hendrix SA. Nanogram nitrite and nitrate determination in environmental and

627   biological materials by vanadium (III) reduction with chemiluminescence detection. Anal Chem.

628   1989 Dec 15;61(24):2715-8. doi: 10.1021/ac00199a007. PMID: 2619057.

629

630   Caley, T., Giraudeau, J., Malaizé, B., Rossignol, L., & Pierre, C. (2012). Agulhas leakage as a

631   key process in the modes of Quaternary climate changes. *Proceedings of the National Academy*

632   *of Sciences of the United States of America*, *109*(18), 6835–6839.

633   https://doi.org/10.1073/pnas.1115545109

634

635   Cartagena-Sierra, A., Berke, M. A., Robinson, R. S., Marcks, B., Castañeda, I. S., Starr, A., Hall,

636   I. R., Hemming, S. R., & LeVay, L. J. (2021). Latitudinal Migrations of the Subtropical Front at

637   the Agulhas Plateau Through the Mid-Pleistocene Transition. *Paleoceanography and*

638   *Paleoclimatology*, *36*(7), e2020PA004084. https://doi.org/10.1029/2020PA004084

639

640   Casciotti, K. L., Sigman, D. M., Hastings, M. G., Böhlke, J. K., & Hilkert, A. (2002).

641   Measurement of the oxygen isotopic composition of nitrate in seawater and freshwater using the

642   denitrifier method. Analytical chemistry, 74(19), 4905-4912. https://doi.org/10.1021/ac020113w

643

644   Chalk, T. B., Hain, M. P., Foster, G. L., Rohling, E. J., Sexton, P. F., Badger, M. P. S., Cherry, S.

645   G., Hasenfratz, A. P., Haug, G. H., Jaccard, S. L., Martínez-García, A., Pälike, H., Pancost, R.

646   D., & Wilson, P. A. (2017). Causes of ice age intensification across the mid-pleistocene

647   transition. *Proceedings of the National Academy of Sciences of the United States of America*,

648   *114*(50), 13114–13119. https://doi.org/10.1073/pnas.1702143114

649

650   Crundwell, M., Scott, G., Naish, T., & Carter, L. (2008). Glacial-interglacial ocean climate

651   variability from planktonic foraminifera during the Mid-Pleistocene transition in the temperate

652   Southwest Pacific, ODP Site 1123. *Palaeogeography, Palaeoclimatology, Palaeoecology*,

653   *260*(1–2), 202–229. https://doi.org/10.1016/j.palaeo.2007.08.023

654

655   Diekmann, B., & Kuhn, G. (2002). Sedimentary record of the mid-Pleistocene climate transition
656   in the southeastern South Atlantic (ODP Site 1090). *Palaeogeography, Palaeoclimatology,*
657   *Palaeoecology*, *182*(3–4), 241–258. https://doi.org/10.1016/S0031-0182(01)00498-9

659   DiFiore, P. J., Sigman, D. M., Karsh, K. L., Trull, T. W., Dunbar, R. B., & Robinson, R. S.
660   (2010). Poleward decrease in the isotope effect of nitrate assimilation across the Southern Ocean.
661   Geophysical Research Letters, 37(17). https://doi.org/10.1029/2010GL044090

663   Dupuy, C., Pagano, M., Got, P., Domaizon, I., Chappuis, A., Marchesseau, G. and Bouvy, M.
664   (2016) Trophic relationships between metazooplankton communities and their plankton food
665   sources in the Iles Eparses (Western Indian Ocean). Marine Environmental Research 116, 18-31.

667   Farmer, J. R., Hönisch, B., Haynes, L. L., Kroon, D., Jung, S., Ford, H. L., Raymo, M. E.,
668   Jaume-Seguí, M., Bell, D. B., Goldstein, S. L., Pena, L. D., Yehudai, M., & Kim, J. (2019). Deep
669   Atlantic Ocean carbon storage and the rise of 100,000-year glacial cycles. *Nature Geoscience*, 1–
670   1. https://doi.org/10.1038/s41561-019-0334-6

672   Ferrari, R., Jansen, M. F., Adkins, J. F., Burke, A., Stewart, A. L., & Thompson, A. F. (2014).
673   Antarctic sea ice control on ocean circulation in present and glacial climates. *Proceedings of the*
674   *National Academy of Sciences of the United States of America*, *111*(24), 8753–8758.
675   https://doi.org/10.1073/pnas.1323922111

677   Ford, B. H. L., & Chalk, T. B. (2020). THE MID-PLEISTOCENE ENIGMA. *Oceanography*,
678   *33*(2), 101–103.

680   Fripiat, F., Martínez-García, A., Fawcett, S. E., Kemeny, P. C., Studer, A. S., Smart, S. M.,
681   Rubach, F., Oleynik, S., Sigman, D. M., & Haug, G. H. (2019). The isotope effect of nitrate
682   assimilation in the Antarctic Zone: Improved estimates and paleoceanographic implications.
683   *Geochimica et Cosmochimica Acta*, *247*, 261–279. https://doi.org/10.1016/j.gca.2018.12.003

685   Garcia, H. E., R. A. Locarnini, T. P. Boyer, J. I. Antonov, O.K. Baranova, M.M. Zweng, J.R.
686   Reagan, D.R. Johnson, 2014. World Ocean Atlas 2013, Volume 4: Dissolved Inorganic Nutrients
687   (phosphate, nitrate, silicate). S. Levitus, Ed., A. Mishonov Technical Ed.; NOAA Atlas NESDIS
688   76, 25 pp.

690   Gonfiantini, R., Stichler, W., & Rozanski, K. (1995). Standards and intercomparison materials
691   distributed by the International Atomic Energy Agency for stable isotope measurements (No.
692   IAEA-TECDOC--825).

694   Haddam, N. A., Michel, E., Siani, G., Cortese, G., Bostock, H. C., Duprat, J. M., & Isguder, G.
695   (2016). Improving past sea surface temperature reconstructions from the Southern Hemisphere
696   oceans using planktonic foraminiferal census data. *Paleoceanography*, *31*(6), 822–837.
697   https://doi.org/10.1002/2016PA002946

699 Harms, N. C., Lahajnar, N., Gaye, B., Rixen, T., Dähnke, K., Ankele, M., Schwarz-Schampera,
700 U., & Emeis, K.-C. (2019). *Nutrient distribution and nitrogen and oxygen isotopic composition*
701 *of nitrate in water masses of the subtropical South Indian Ocean.* https://doi.org/10.5194/bg-
702 2018511

704 Hasenfratz, A. P., Jaccard, S. L., Martínez-García, A., Sigman, D. M., Hodell, D. A., Vance, D.,
705 Bernasconi, S. M., Kleiven, H. F., Haumann, F. A., & Haug, G. H. (2019). The residence time of
706 Southern Ocean surface waters and the 100,000-year ice age cycle. *Science*, 1080–1084.
707 https://doi.org/10.1126/science.aat7067

709 Hönisch, B., Hemming, N., Archer, D., Siddall, M., & McManus, J. (2009). Atmospheric Carbon
710 Dioxide Concentration Across the Mid-Pleistocene Transition. *Science (New York, N.Y.)*, *324*,
711 1551–1554. https://doi.org/10.1126/science.1171477

713 Hoogakker, B. A. A., Rohling, E. J., Palmer, M. R., Tyrrell, T., & Rothwell, R. G. (2006).
714 Underlying causes for long-term global ocean δ13C fluctuations over the last 1.20 Myr. *Earth*
715 *and Planetary Science Letters*, *248*(1–2), 15–29. https://doi.org/10.1016/j.epsl.2006.05.007

717 Jaccard, S. L., Hayes, C. T., Martínez-García, A., Hodell, D. A., Anderson, R. F., Sigman, D. M.,
718 & Haug, G. H. (2013). Two Modes of Change in Southern Ocean Productivity Over the Past
719 Million Years. *Science*, *339*(6126), 1419–1423. https://doi.org/10.1126/SCIENCE.1227545

721 Jonkers, L., & Kučera, M. (2015). Global analysis of seasonality in the shell flux of extant
722 planktonic Foraminifera. Biogeosciences, 12(7), 2207-2226. https://doi.org/10.5194/bg-12-2207-
723 2015

725 Kaiser, E. A., Billups, K., & Bradtmiller, L. (2021). A 1 Million Year Record of Biogenic Silica
726 in the Indian Ocean Sector of the Southern Ocean: Regional Versus Global Forcing of Primary
727 Productivity. *Paleoceanography and Paleoclimatology*, *36*(3), e2020PA004033.
728 https://doi.org/10.1029/2020PA004033

730 Kemp, A. E. S., Grigorov, I., Pearce, R. B., & Naveira Garabato, A. C. (2010). Migration of the
731 Antarctic Polar Front through the mid-Pleistocene transition: Evidence and climatic implications.
732 *Quaternary Science Reviews*, *29*(17–18), 1993–2009.
733 https://doi.org/10.1016/j.quascirev.2010.04.027

735 Kennett, J.P., Srinivasan, M. (1983). Neogene Planktonic Foraminifera: A Phylogenetic Atlas.
736 Hutchinson Ross, Stroudsburg (273 pp).

738 Khatiwala, S., Schmittner, A., & Muglia, J. (2019). Air-sea disequilibrium enhances ocean
739 carbon storage during glacial periods. *Science Advances*, *5*(6), eaaw4981–eaaw4981.
740 https://doi.org/10.1126/sciadv.aaw4981
741

742 Kim, J. E., Khim, B. K., Ikehara, M., & Lee, J. (2018). Orbital-scale denitrification changes in the
743 Eastern Arabian Sea during the last 800 kyrs. Scientific Reports, 8(1), 1-8.
744 https://doi.org/10.1016/j.margen.2021.100849
745
746 King, A. L., & Howard, W. R. (2003). Planktonic foraminiferal flux seasonality in Subantarctic
747 sediment traps: A test for paleoclimate reconstructions. Paleoceanography, 18(1).
748 https://doi.org/10.1029/2002PA000839
749
750 Knapp, A. N., Sigman, D. M., and Lipschultz, F. (2005), N isotopic composition of dissolved
751 organic nitrogen and nitrate at the Bermuda Atlantic Time-series Study site, Global Biogeochem.
752 Cycles, 19, GB1018, doi:10.1029/2004GB002320.
753
754 Kolasinski, J., Kaehler, S. and Jaquemet, S. (2012) Distribution and sources of particulate organic
755 matter in a mesoscale eddy dipole in the Mozambique Channel (south-western Indian Ocean):
756 Insight from C and N stable isotopes. Journal of Marine Systems 96-97, 122-131.
757
758 Kretschmer, K., Jonkers, L., Kucera, M., & Schulz, M. (2018). Modeling seasonal and vertical
759 habitats of planktonic foraminifera on a global scale. Biogeosciences, 15(14), 4405-4429.
760 https://doi.org/10.5194/bg-15-4405-2018
761
762 Laskar, J., Robutel, P., Joutel, F., Gastineau, M., Correia, A. C. M., & Levrard, B. (2004). A
763 long-term numerical solution for the insolation quantities of the Earth. Astronomy &
764 Astrophysics, 428(1), 261-285.
765
766 Lear, C. H., Billups, K., Rickaby, R. E. M., Diester-Haass, L., Mawbey, E. M., & Sosdian, S. M.
767 (2016). Breathing more deeply: Deep ocean carbon storage during the mid-Pleistocene climate
768 transition. *GEOLOGY*, *44*. https://doi.org/10.1130/G38636.1
769
770 Li, F., Ginoux, P., & Ramaswamy, V. (2008). Distribution, transport, and deposition of mineral
771 dust in the Southern Ocean and Antarctica: Contribution of major sources. *Journal of
772 Geophysical Research: Atmospheres*, *113*(D10). https://doi.org/10.1029/2007JD009190
773
774 Lisiecki, L. E. (2010). Links between eccentricity forcing and the 100,000-year glacial cycle.
775 *Nature Geoscience*, *3*(5), 349–352. https://doi.org/10.1038/ngeo828
776
777 Loeblich, A., Tappan, H., 1988. Foraminiferal Genera and Their Classification. 2. van Nostrand
778 Reinhold Company Publisher, pp. 1–212.
779
780 Maiorano, P., Marino, M., & Flores, J.-A. (2009). The warm interglacial Marine Isotope Stage
781 31: Evidences from the calcareous nannofossil assemblages at Site 1090 (Southern Ocean).
782 *Marine Micropaleontology*, *71*(3–4), 166–175. https://doi.org/10.1016/j.marmicro.2009.03.002
783
784 Marcks, Basia; Santos, Thiago Pereira dos; Lessa, Douglas Villela de Oliveira; Cartagena-Sierra,
785 Alejandra; Berke, Melissa A; Starr, Aidan; Hall, Ian R; Kelly, Roger P; Robinson, Rebecca S

786 (2022a): δ¹⁵N in planktonic foraminifera species G. bulloides and G. inflata from IODP Site 361-
787 U1475. [Dataset], PANGAEA, https://doi.org/10.1594/PANGAEA.945839

789 Marcks, Basia; Santos, Thiago Pereira dos; Lessa, Douglas Villela de Oliveira; Cartagena-Sierra,
790 Alejandra; Berke, Melissa A; Starr, Aidan; Hall, Ian R; Kelly, Roger P; Robinson, Rebecca S
791 (2022b): Abundance of Neogloboquadrina pachyderma sinistral from IODP Site 361-U1475.
792 [Dataset], PANGAEA, https://doi.org/10.1594/PANGAEA.945840

794 Marcks, Basia; Santos, Thiago Pereira dos; Lessa, Douglas Villela de Oliveira; Cartagena-Sierra,
795 Alejandra; Berke, Melissa A; Starr, Aidan; Hall, Ian R; Kelly, Roger P; Robinson, Rebecca S
796 (2022c): Opal mass accumulation rates from IODP Site 361-U1475. [Dataset], PANGAEA,
797 https://doi.org/10.1594/PANGAEA.945841

799 Marshall, J., & Speer, K. (2012). Closure of the meridional overturning circulation through
800 Southern Ocean upwelling. Nature Geoscience, 5(3), 171-180.

802 Martin, J. H. (1990). Glacial-interglacial CO2 change: The Iron Hypothesis. *Paleoceanography*,
803 *5*(1), 1–13. https://doi.org/10.1029/PA005i001p00001

805 Martínez-García, A., Rosell-Melé, A., Geibert, W., Gersonde, R., Masqué, P., Gaspari, V., &
806 Barbante, C. (2009). Links between iron supply, marine productivity, sea surface temperature,
807 and CO 2 over the last 1.1 Ma. *Paleoceanography*, *24*(1). https://doi.org/10.1029/2008PA001657

809 Martínez-García, A., Rosell-Melé, A., Jaccard, S. L., Geibert, W., Sigman, D. M., & Haug, G. H.
810 (2011). Southern Ocean dust-climate coupling over the past four million years. *Nature*,
811 *476*(7360), 312–315. https://doi.org/10.1038/nature10310

813 Martínez-García, A., Rosell-Mele, A., McClymont, E. L., Gersonde, R., & Haug, G. H. (2010).
814 Subpolar Link to the Emergence of the Modern Equatorial Pacific Cold Tongue. *Science*,
815 *328*(5985), 1550–1553. https://doi.org/10.1126/science.1184480

817 Martínez-García, A., Sigman, D. M., Ren, H., Anderson, R. F., Straub, M., Hodell, D. A.,
818 Jaccard, S. L., Eglinton, T. I., & Haug, G. H. (2014). Iron fertilization of the subantarctic ocean
819 during the last ice age. *Science*, *343*(6177), 1347–1350. https://doi.org/10.1126/science.1246848

821 McKay, R., Naish, T., Carter, L., Riesselman, C., Dunbar, R., Sjunneskog, C., Winter, D.,
822 Sangiorgi, F., Warren, C., Pagani, M., Schouten, S., Willmott, V., Levy, R., DeConto, R., &
823 Powell, R. D. (2012). Antarctic and Southern Ocean influences on Late Pliocene global cooling.
824 *Proceedings of the National Academy of Sciences*, *109*(17), 6423–6428.
825 https://doi.org/10.1073/pnas.1112248109

827 Monterey, G. I., & Levitus, S. (1997). Climatological cycle of mixed layer depth in the world
828 ocean, report, 5 pp., NOAA, Silver Spring, Md. In NOAA Atlas NESDIS 14, Silver spring. Md:
829 National Oceanic and Atmospheric Administration.

831   Mortlock, R. A., & Froelich, P. N. (1989). A simple method for the rapid determination of
832   biogenic opal in pelagic marine sediments. Deep Sea Research Part A. Oceanographic Research
833   Papers, 36(9), 1415-1426. https://doi.org/10.1016/0198-0149(89)90092-7
834

835   Muglia, J., Skinner, L. C., & Schmittner, A. (2018). Weak overturning circulation and high
836   Southern Ocean nutrient utilization maximized glacial ocean carbon. *Earth and Planetary
837   Science Letters*, *496*, 47–56. https://doi.org/10.1016/J.EPSL.2018.05.038
838

839   Nydahl & Folke (1978) On the peroxodisulfate oxidation of total nitrogen in waters to nitrate:
840   Water Research, v. 12, p. 1123–1130. https://doi.org/10.1016/0043-1354(78)90060-X
841

842   Olbers, D., Gouretsky, V., Seiß, G., & Schröter, J. (1992). Hydrographic Atlas of the Southern
843   Ocean. In *Alfred-Wegener-Institut, Bremerhaven*. https://epic.awi.de/id/eprint/2325/
844

845   Orsi, A. H., Whitworth, T., & Nowlin, W. D. (1995). On the meridional extent and fronts of the
846   Antarctic Circumpolar Current. *Deep Sea Research Part I: Oceanographic Research Papers*,
847   *42*(5), 641–673. https://doi.org/10.1016/0967-0637(95)00021-W
848

849   Peeters, F. J. C., Acheson, R., Brummer, G. J. A., De Ruijter, W. P. M., Schneider, R. R.,
850   Ganssen, G. M., Ufkes, E., & Kroon, D. (2004). Vigorous exchange between the Indian and
851   Atlantic oceans at the end of the past five glacial periods. *Nature*, *430*(7000), 661–665.
852   https://doi.org/10.1038/nature02785
853

854   Pena, L. D., & Goldstein, S. L. (2014). *Thermohaline circulation crisis and impacts during the
855   mid-Pleistocene transition*. *Science* 345.6194 (2014): 318-322.
856   https://doi.org/10.1126/science.1249770
857

858   Ren, H., Sigman, D. M., Meckler, A. N., Plessen, B., Robinson, R. S., Rosenthal, Y., & Haug, G.
859   H. (2009). Foraminiferal isotope evidence of reduced nitrogen fixation in the ice age Atlantic
860   ocean. *Science*, *323*(5911), 244–248. https://doi.org/10.1126/science.1165787
861

862   Robinson, R., Sigman, D., Difiore, P., Rohde, M., Mashiotta, T., Lea, D., & Robinson, C. (2005).
863   Diatom-bound 15N/14N: New support for enhanced nutrient consumption in the ice age
864   Subantarctic. *Paleoceanography*, *20*. https://doi.org/10.1029/2004PA001114
865

866   Robinson, R. S., Jones, C. A., Kelly, R. P., Rafter, P., Etourneau, J., & Martinez, P. (2019). A
867   cool, nutrient-enriched eastern equatorial Pacific during the mid-Pleistocene transition.
868   Geophysical Research Letters, 46(4), 2187-2195. https://doi.org/10.1029/2018GL081315
869

870   *RStudio Team (2020). RStudio: Integrated Development for R. RStudio, PBC, Boston, MA URL
871   http://www.rstudio.com/*.
872

873 Russell, J. L., Dixon, K. W., Gnanadesikan, A., Stouffer, R. J., & Toggweiler, J. R. (2006). The
874 Southern Hemisphere westerlies in a warming world: Propping open the door to the deep ocean.
875 Journal of Climate, 19(24), 6382-6390.
876
877 Sigman, D. M., Altabet, M. A., Francois, R., McCorkle, D. C., & Gaillard, J.-F. (1999). The
878 isotopic composition of diatom-bound nitrogen in Southern Ocean sediments.
879 *Paleoceanography*, *14*(2), 118–134. https://doi.org/10.1029/1998PA900018
880
881 Sigman,D. M., Casciotti, K. L., Andreani, M., Barford, C., Galanter, M., and Böhlke, J. K.,
882 (2001). A Bacterial Method for the Nitrogen Isotopic Analysis of Nitrate in Seawater and
883 Freshwater. *Analytical Chemistry*, 73(17), 4145-4153. DOI: 10.1021/ac010088e
884
885 Sigman, D. M., Hain, M. P., & Haug, G. H. (2010). The polar ocean and glacial cycles in
886 atmospheric CO2 concentration. *Nature*, *466*(7302), 47–55. https://doi.org/10.1038/nature09149
887
888 Sigman, D. M., Fripiat, F., Studer, A. S., Kemeny, P. C., Martínez-García, A., Hain, M. P., ... &
889 Haug, G. H. (2021). The Southern Ocean during the ice ages: A review of the Antarctic surface
890 isolation hypothesis, with comparison to the North Pacific. Quaternary Science Reviews, 254,
891 106732.
892
893 Simon, M. H., Arthur, K. L., Hall, I. R., Peeters, F. J. C., Loveday, B. R., Barker, S., Ziegler, M.,
894 & Zahn, R. (2013). Millennial-scale Agulhas Current variability and its implications for
895 saltleakage through the Indian-Atlantic Ocean Gateway. *Earth and Planetary Science Letters*,
896 *383*, 101–112. https://doi.org/10.1016/j.epsl.2013.09.035
897
898 Smart, S. M., Fawcett, S. E., Ren, H., Schiebel, R., Tompkins, E. M., Martínez-García, A.,
899 Stirnimann, L., Roychoudhury, A., Haug, G. H., & Sigman, D. M. (2020). The nitrogen isotopic
900 composition of tissue and shell-bound organic matter of planktic foraminifera in Southern Ocean
901 surface waters. *Geochemistry, Geophysics, Geosystems*, *21*(2).
902 https://doi.org/10.1029/2019gc008440
903
904 Starr, A., Hall, I. R., Barker, S., Rackow, T., Zhang, X., Hemming, S. R., van der Lubbe, H. J.
905 L., Knorr, G., Berke, M. A., Bigg, G. R., Cartagena-Sierra, A., Jiménez-Espejo, F. J., Gong, X.,
906 Gruetzner, J., Lathika, N., LeVay, L. J., Robinson, R. S., Ziegler, M., Brentegani, L., … Zhang,
907 H. (2021). Antarctic icebergs reorganize ocean circulation during Pleistocene glacials. *Nature*,
908 *589*(7841), 236–241. https://doi.org/10.1038/s41586-020-03094-7
909
910 Tangunan, D., M. A. Berke, A. Cartagena-Sierra, J. A. Flores, J. Gruetzner, F. Jiménez-Espejo, L.
911 J. LeVay, K.-H. Baumann, O. Romero, and M. Saavedra-Pellitero (2021), Strong glacial-
912 interglacial variability in upper ocean hydrodynamics, biogeochemistry, and productivity in the
913 southern Indian Ocean, Communications Earth & Environment, 2(1), 1-13.
914 https://doi.org/10.1038/s43247-021-00148-0
915

916   Toggweiler, J. R., Russell, J. L., & Carson, S. R. (2006). Midlatitude westerlies, atmospheric
917   CO2, and climate change during the ice ages. Paleoceanography, 21(2).
918
919   van Sebille, E., Scussolini, P., Durgadoo, J. V., Peeters, F. J., Biastoch, A., Weijer, W., ... &
920   Zahn, R. (2015). Ocean currents generate large footprints in marine palaeoclimate proxies. Nature
921   communications, 6(1), 1-8. https://doi.org/10.1038/ncomms7521
922
923
924   Wang, P., Tian, J., Cheng, X., Liu, C., & Xu, J. (2004). Major Pleistocene stages in a carbon
925   perspective: The South China Sea record and its global comparison. *Paleoceanography*, *19*(4),
926   n/a-n/a. https://doi.org/10.1029/2003PA000991
927
928   Yang, H., Lohmann, G., Krebs-Kanzow, U., Ionita, M., Shi, X., Sidorenko, D., Gong, X., Chen,
929   X., & Gowan, E. J. (2020). Poleward Shift of the Major Ocean Gyres Detected in a Warming
930   Climate. *Geophysical Research Letters*, *47*(5), e2019GL085868.
931   https://doi.org/10.1029/2019GL085868
932
933   Zahn, R. (2009). Beyond the CO2 connection. *Nature*, *460*(7253), 335–336.
934   https://doi.org/10.1038/46

935

DRAFT